

Lithium in the lower red giant branch of 5 Galactic globular clusters^{★,★★}

C. Aguilera-Gómez^{1,2}, L. Monaco¹, A. Mucciarelli^{3,4}, M. Salaris⁵, S. Villanova⁶, and E. Pancino⁷

¹ Departamento de Ciencias Físicas, Universidad Andres Bello, Fernandez Concha 700, Las Condes, Santiago, Chile
e-mail: craguile@uc.cl

² Núcleo de Astronomía, Universidad Diego Portales, Ejército 441, Santiago, Chile

³ Dipartimento di Fisica e Astronomia, Università degli Studi di Bologna, Via Gobetti 93/2, I-40129 Bologna, Italy

⁴ INAF - Osservatorio di Astrofisica e Scienza dello Spazio di Bologna, Via Gobetti 93/3, I-40129 Bologna, Italy

⁵ Astrophysics Research Institute, Liverpool John Moores University, IC2, Liverpool Science Park, 146 Brownlow Hill, Liverpool, L3 5RF, UK

⁶ Departamento de Astronomía, Casilla 160-C, Universidad de Concepción, Chile

⁷ INAF - Osservatorio Astrofisico di Arcetri, Largo Enrico Fermi 5, I-50125 Firenze, Italy

Received ; accepted

ABSTRACT

Context. Lithium is one of the few elements produced during the Big Bang Nucleosynthesis in the early universe. Moreover, its fragility makes it useful as a proxy for stellar environmental conditions. As such, the lithium abundance in old systems is at the core of different astrophysical problems.

Aims. Stars in the lower red giant branch allow studying globular clusters where main sequence stars are too faint to be observed. We use these stars to analyze the initial Li content of the clusters and compare it to cosmological predictions, to measure spreads in Li between different stellar populations, and to study signs of extra depletion in these giants.

Methods. We use GIRAFFE spectra to measure the lithium and sodium abundances of lower red giant branch stars in 5 globular clusters. These cover an extensive range in metallicity, from $[\text{Fe}/\text{H}] \sim -0.7$ to $[\text{Fe}/\text{H}] \sim -2.3$ dex.

Results. We find that the lithium abundance in these lower red giant branch stars forms a plateau, with values from $A(\text{Li})_{\text{NLTE}} = 0.84$ to 1.03 dex, showing no clear correlation with metallicity. When using stellar evolutionary models to calculate the primordial abundance of these clusters, we recover values $A(\text{Li})_{\text{NLTE}} = 2.1 - 2.3$ dex, consistent with the constant value observed in warm metal-poor halo stars, the Spite plateau. Additionally, we find no difference in the lithium abundance of first and second population stars in each cluster. We also report the discovery of a Li-rich giant in the cluster NGC3201, with $A(\text{Li})_{\text{NLTE}} = 1.63 \pm 0.18$ dex, where the enrichment mechanism is probably pollution from external sources.

Key words. globular clusters: general – stars: abundances – primordial nucleosynthesis – stars: chemically peculiar

1. Introduction

Lithium (Li) is one of the few elements that are produced minutes after the Big Bang during the Big Bang Nucleosynthesis phase (BBN, Coc et al. 2014). Predictions of the production of elements in this theory are only dependent on the baryon-to-photon ratio, a number that has been measured from the cosmic microwave background by WMAP (Hinshaw et al. 2013) and Planck (Planck Collaboration et al. 2014). Then, the predicted amount of lithium formed in the early universe is $A(\text{Li})^1 = 2.69 \pm 0.03$ (Coc et al. 2014). The primitive lithium abundance, to be compared with predictions from the BBN, is measured from old, metal-poor halo stars. This value is expected to be indicative of the primordial abundance, since stars this metal-poor do not have enough time at formation to be enriched with material from the interstellar medium or galactic sources producing Li (e.g. Prantzos 2012). Spite & Spite (1982a,b) found that halo

dwarf stars with $[\text{Fe}/\text{H}]$ between -2.4 and -1.4 dex and effective temperatures between 5700 and 6300 K share a similar abundance of $A(\text{Li}) = 2.2$ dex, the so-called *Spite Plateau*, a result that has been confirmed in the halo (e.g. Charbonnel & Primas 2005; Meléndez et al. 2010) and in other environments, such as globular clusters (e.g. Bonifacio 2002). The discrepancy between the predicted $A(\text{Li})$ from the BBN and the measurements, over 3 times lower, is referred to as the *Cosmic Lithium Problem*. Notice that Lithium is the only measured element produced during the BBN that experiences such a discrepancy (Coc et al. 2014).

Moreover, to further complicate the picture, there is a decrease in the mean Li abundance and an increase in scatter at the lower-end metallicity of the Spite plateau, for metallicities $[\text{Fe}/\text{H}] < -2.8$, known as the *meltdown* (Sbordone et al. 2010, and references therein), although some puzzling very metal-poor stars have been found with higher Li abundances, closer to the plateau (e.g. Bonifacio et al. 2018; Aguado et al. 2019).

Solutions for the discrepancy between Li measurements and predictions from BBN range from modifications to the BBN theory to processes affecting the stellar interiors and changing the Li abundance in old stars (see Fields 2011, for a review).

[★] Based on observations collected at the European Southern Observatory under ESO programme 095.D-0735(A).

^{★★} Table A.1 is available in electronic form at the CDS via anonymous ftp to cdsarc.u-strasbg.fr (130.79.128.5) or via <http://cdsweb.u-strasbg.fr/cgi-bin/qcat?J/A+A/>

¹ $A(\text{Li}) = \log(n_{\text{Li}}/n_{\text{H}}) + 12$

Lithium is an element often used as an indicator of chemical processes affecting the interior of stars, such as mixing, since it burns at temperatures (2.5×10^6 K) and densities found in main-sequence stars. Thus, it is possible that a process such as diffusion (Fu et al. 2015) or additional turbulent mixing (Richard et al. 2005) is depleting the abundance in the stellar atmospheres of old stars which would not be indicative of the BBN lithium.

Metal-poor globular clusters are among the oldest objects in the Galaxy (e.g. De Angeli et al. 2005). As such, their lithium should resemble closely the abundance produced during BBN, making these systems important probes and tools to study the Cosmic Lithium Problem. However, the measurement of Li abundance requires high quality spectra not easily obtained for the majority of cluster main sequence stars that are too faint. Thus, the Li abundance is known for dwarfs only for a handful of galactic clusters: M4 (Mucciarelli et al. 2011; Monaco et al. 2012), NGC6397 (Lind et al. 2009b; González Hernández et al. 2009), NGC 7099 (Gruyters et al. 2016), NGC6752 (Pasquini et al. 2005; Shen et al. 2010), 47 Tuc (D’Orazi et al. 2010; Dobrovolskas et al. 2014), Omega Centauri (Monaco et al. 2010), and M92 (Bonifacio 2002). In most of these clusters, the Li measured closely resembles that of the Spite Plateau, with the exception of 47 Tuc.

Additionally, globular clusters, once thought to be defined chemically by a single population of stars, with no dispersion in chemical abundances are now known to harbor populations with different light element abundances (Bastian & Lardo 2018). The second population of stars, which according to current scenarios would be born from the processed material from the first population, have high [Na/Fe] and low [O/Fe] producing the observed Sodium-Oxygen anticorrelation in globular clusters (Carretta et al. 2009b,c). Given that the thermonuclear reactions that produce this pattern occur at higher temperatures than that required to burn Li, it is expected that a second population of stars should have a lower Li than the first population. However, only two clusters, with Li measured in their main sequence, show a hint of a Li-O correlation, 47 Tuc (Dobrovolskas et al. 2014), with no Li-Na anticorrelation, and NGC6752 (Shen et al. 2010). In M4 there is a weak but statistically significant Li-Na anticorrelation (Monaco et al. 2012), while other clusters are shown to have similar Li in first and second population stars. The lack of a Li anticorrelation could be produced if the polluter of the second population has a significant Li production or if the material from the polluter is mixed with unprocessed material that preserved its initial lithium. Thus, studying the Li in globular clusters can aid to understand their formation.

The lack of more Li measurements in main sequence stars of globular clusters due to their faintness encourages the use of a complementary method, proposed by Mucciarelli et al. (2012), which uses lower red giant branch stars (LRGB).

Red giant stars undergo a series of structural changes that produce alterations to their surface chemical abundances. The first of these processes is the *first dredge-up* (FDU), where the surface convective envelope of the stars deepens in mass, mixing material from the surface with the chemically processed interior. This translates into a decrease in the carbon and lithium abundances and an increase in the nitrogen abundance.

Standard stellar evolutionary models predict no other surface abundance changes in the red giant branch (RGB) after the end of the FDU. However, observations provide evidence of modified Li, C, N, O abundances and C isotopic ratio after the RGB bump (Gratton et al. 2000). At this moment in stellar evolution, the advancing hydrogen-burning shell encounters and erases the discontinuity left in the chemical profile of the star by the deep-

est penetration of the convective envelope (Denissenkov & Vandenberg 2003), allowing extra-mixing to proceed (or do so more efficiently, e.g. Chanamé et al. 2005) bringing material from the stellar interior to the surface. The details of how this mechanism acts and how it affects the stellar interiors are, however, not well understood.

LRGBs are located between the end of the first dredge-up and the luminosity function bump. The dilution of lithium during the FDU at the beginning of the red giant phase is mass and metallicity dependent, but it is well characterized by stellar evolutionary models. This is why a complementary way to study Li in old stars is to measure its abundance in LRGBs, where the $A(\text{Li})$ is constant at a given metallicity, mirroring the Spite-plateau but at a lower value of $A(\text{Li}) \sim 0.9 - 1.0$ dex that considers its depletion in the FDU. Moreover, the FDU mitigates the effects of diffusion, one of the main uncertainties for the interpretation of the Li abundance in dwarfs (Mucciarelli et al. 2011).

Mucciarelli et al. (2014) used this technique to study the primordial Li abundance of the globular cluster M54 located in the Sagittarius dwarf Spheroidal galaxy, providing evidence that the primordial Li is the same there as in the Milky Way and thus, that the *Cosmic lithium problem* is Universal and not local. More evidence for this can be found in ω Cen, usually considered to be the remnant core of an accreted galaxy (e.g. Lee et al. 1999; Pancino et al. 2000), that also shows a consistent Li abundance with the Spite plateau (Monaco et al. 2010). The discovery of Gaia-Enceladus, a disrupted dwarf galaxy that was once accreted by the Milky Way, and is now forming part of the galactic halo, allows a new way to study the primordial Li content outside our Galaxy, confirming once again, the universality of the cosmic Li problem (Molaro et al. 2020; Simpson et al. 2021).

Confirming that the LRGB stars can also be used to study the formation of globular clusters, Mucciarelli et al. (2018) measure Li in LRGB stars of ω Cen, finding an extended Na-Li anticorrelation. However, this distribution seems to be rather complex, with the most metal-rich stars in the cluster always showing low Li abundances, but the metal-poor stars in the cluster can either show low sodium and normal Li, or high sodium with normal or depleted Li abundances.

Thus, as demonstrated by these works, the study of LRGBs allows to characterize the Li abundance pattern of clusters and the primordial Li in systems where dwarfs are too faint. Following this complementary approach, in this work we study the Li abundance of lower red giant branch stars of 5 Galactic globular clusters, providing new insight in the dependence of the RGB Li plateau with metallicity and its use to calculate the primordial Li abundance in these systems.

Moreover, one of these clusters, NGC6838 is a metal-rich globular cluster. The low Li abundance of dwarfs in the relatively metal-rich cluster 47 Tuc ($[\text{Fe}/\text{H}] = -0.8$ dex and $A(\text{Li}) = 1.4 - 2.2$ dex, Dobrovolskas et al. 2014) when compared to the Spite plateau suggest that there is a depletion mechanism acting in the main sequence at higher metallicities, that is not found at lower metallicities, given that M4, with $[\text{Fe}/\text{H}] = -1.1$ dex shows Li consistent with the Spite plateau (Monaco et al. 2012). The study of NGC6838 will allow us to test if this is a peculiar pattern for 47 Tuc or if all metal-rich globular clusters are Li depleted.

Also notice that NGC3201 is significantly younger (~ 2 Gyr) than the rest of the studied clusters (Marín-Franch et al. 2009).

In Section 2 we report the observations and evaluate membership of our targets to the globular clusters. We measure atmospheric parameters (Section 3) and lithium and sodium abundances (Section 4) of these stars. We report results on the LRGB Li plateau, on the lack of a Li-Na correlation in these clusters,

and on the discovery of a new Li-rich giant in NGC3201 in Section 5. Our summary can be found in Section 6.

2. Observations and membership

We selected five clusters in order to cover the entire metallicity range of Halo globular clusters, and observe a large number of stars. We end up with NGC4590 (M 68), NGC6809 (M 55), NGC6656 (M 22), NGC3201, and NGC6838 (M 71). For each of these 5 clusters we selected our targets in the LRGB phase. The spectroscopic observations correspond to the ESO program 095.D-0735 (PI. A. Mucciarelli) and were carried out using the FLAMES multi-object spectrograph (Pasquini et al. 2002) at the Very Large Telescope (VLT). The GIRAFFE fibers provide mid-resolution spectra with $R \sim 18000$. The observations were performed in the setups HR15N, sampling the lithium resonance doublet at $\lambda \sim 6708 \text{ \AA}$, and HR12, sampling the sodium D doublet at $\lambda \sim 5890 - 5896 \text{ \AA}$ for GIRAFFE.

A total of five exposures, 45 minutes each, for NGC6838, NGC6809, NGC6656, and NGC3201, and, 10 exposures for NGC4590 were taken in the HR15N setup. Only one exposure for each star was needed in the HR12 setup, as the large equivalent width of the Na doublet requires smaller signal-to-noise ratios to be measured.

The spectra were bias-subtracted, flat-fielded and wavelength-calibrated using the standard ESO pipelines². In each exposure, some fibers were dedicated to measure spectra of the sky. These are median-combined to create a master sky, then subtracted to each of our science spectra.

Radial velocities for each individual spectra in the HR15N setup are measured using the IRAF³ task *fxcor*. This task uses the cross correlation method, where we use as template a synthetic spectrum from Coelho et al. (2005), typical of a metal-poor red giant, with a resolution reduced to be similar to our spectra. The typical radial velocity precision is $\sim 2-3 \text{ km s}^{-1}$ for each HR15N spectra of each star. This value is the formal *fxcor* error, related to the fitted function used to calculate the velocity (Tonry & Davis 1979). After shifting every spectrum to their rest-frame, we median-combine all spectra that correspond to a particular target to obtain an individual spectrum for each star that is later used in the analysis. By combining all the exposures we obtain an additional error in the radial velocity, corresponding to the standard deviation of different measurements for the same target. These are typically from $\sim 0.6 - 2.2 \text{ km s}^{-1}$. Signal-to-noise ratios per pixel (S/N) in the HR15N setup are typically around $\sim 70 - 300$, while the single exposure for the HR12 allows to obtain spectra with $S/N \sim 20 - 70$. Given the lower S/N of these spectra and the fewer number of lines clearly visible, we do not measure a radial velocity from this setup, but instead assume the average radial velocity measured from the HR15N spectra.

After obtaining a unique radial velocity for each target star, we use these values to construct radial velocity distributions in each cluster. These are fitted with a Gaussian profile, where a mean and a standard deviation are calculated and used as criteria for membership.

Table 1. Mean radial velocity (RV) for each cluster.

Cluster	Mean RV (km s^{-1})	SD (km s^{-1})	Harris RV (km s^{-1})	Harris SD (km s^{-1})
NGC4590	-94.2	3.2	-94.7	2.5
NGC6809	174.9	4.6	174.7	4.0
NGC6656	-146.5	7.8	-146.3	7.8
NGC3201	495.0	3.8	494.0	5.0
NGC6838	-22.9	3.5	-22.8	2.3

Notes. Mean radial velocity (RV) for each cluster and standard deviation (SD) of each radial velocity distribution and comparisons with Harris (1996, 2010 edition).

2.1. Cluster membership

For each cluster, we exclude stars with radial velocities significantly different with respect to the mean radial velocity of the sample stars (a difference higher than 3σ). Additionally, we use the membership probability reported for each star in these clusters by Vasiliev & Baumgardt (2021) which makes use of the Early Data Release 3 for the Gaia mission (Gaia Collaboration et al. 2018), considering that stars are members if they have a membership probability $P_{\text{mem}} > 0.9$.

The cluster NGC6838 is in a particularly contaminated field. With a gaussian distribution we get the mean radial velocity of the cluster and remove all the stars outside 2σ as field contaminants. Only 35 out of 117 observed stars are within that radial velocity range and have astrometric parameters consistent with the cluster.

In NGC6809, from the originally observed 110 stars, 95 remain after excluding stars by their membership probability or radial velocity. In NGC6656, 101 of the 112 observed stars are consistent with being cluster members. In NGC4590, we kept 50 of 69 observed stars, and in NGC3201, 98 out of the 117 observed stars are consistent with the cluster membership.

All of our measured mean radial velocities are reported in Table 1 and are consistent with those in the catalog by Harris (1996, 2010 edition).

3. Atmospheric Parameters

Effective temperatures for stars are derived photometrically, using the (V-I) colour and the Alonso et al. (1999) relations. For all of our clusters, we use the photometry of Stetson et al. (2019) and transform to Johnson (V-I) colors using the relation in Bessell (1983).

To calculate dereddened colors, we use extinction coefficients from McCall (2004). The adopted colour excess $E(B-V)$ and distance modulus for each cluster can be found in Table 2.

Although the color excess of NGC6838 is high, it does not suffer from significant differential reddening ($\langle \delta E(B-V) \rangle = 0.035 \text{ mag}$, Bonatto et al. 2013). For the clusters NGC6656 and NGC3201 we corrected for differential reddening using the maps of Alonso-García et al. (2012) with zero point $E(B-V) = 0.33$ (Schlegel et al. 1998) for NGC6656, as suggested by that work, and of Pancino et al., (in preparation), with zero point $E(B-V) = 0.24$ for NGC3201 (Bonatto et al. 2013).

The surface gravity was calculated for each star using isochrone fitting and a set of MIST isochrones (Dotter 2016; Choi et al. 2016) restricting ages to be higher than 12 Gyr. In particular, we placed the star in an effective temperature - absolute magnitude plane and compare its position there with the theoretical isochrones, using the estimated metallicity of the cluster

² <http://www.eso.org/sci/software/pipelines/>

³ IRAF is distributed by the National Optical Astronomy Observatories, which are operated by the Association of Universities for Research in Astronomy, Inc., under cooperative agreement with the National Science Foundation.

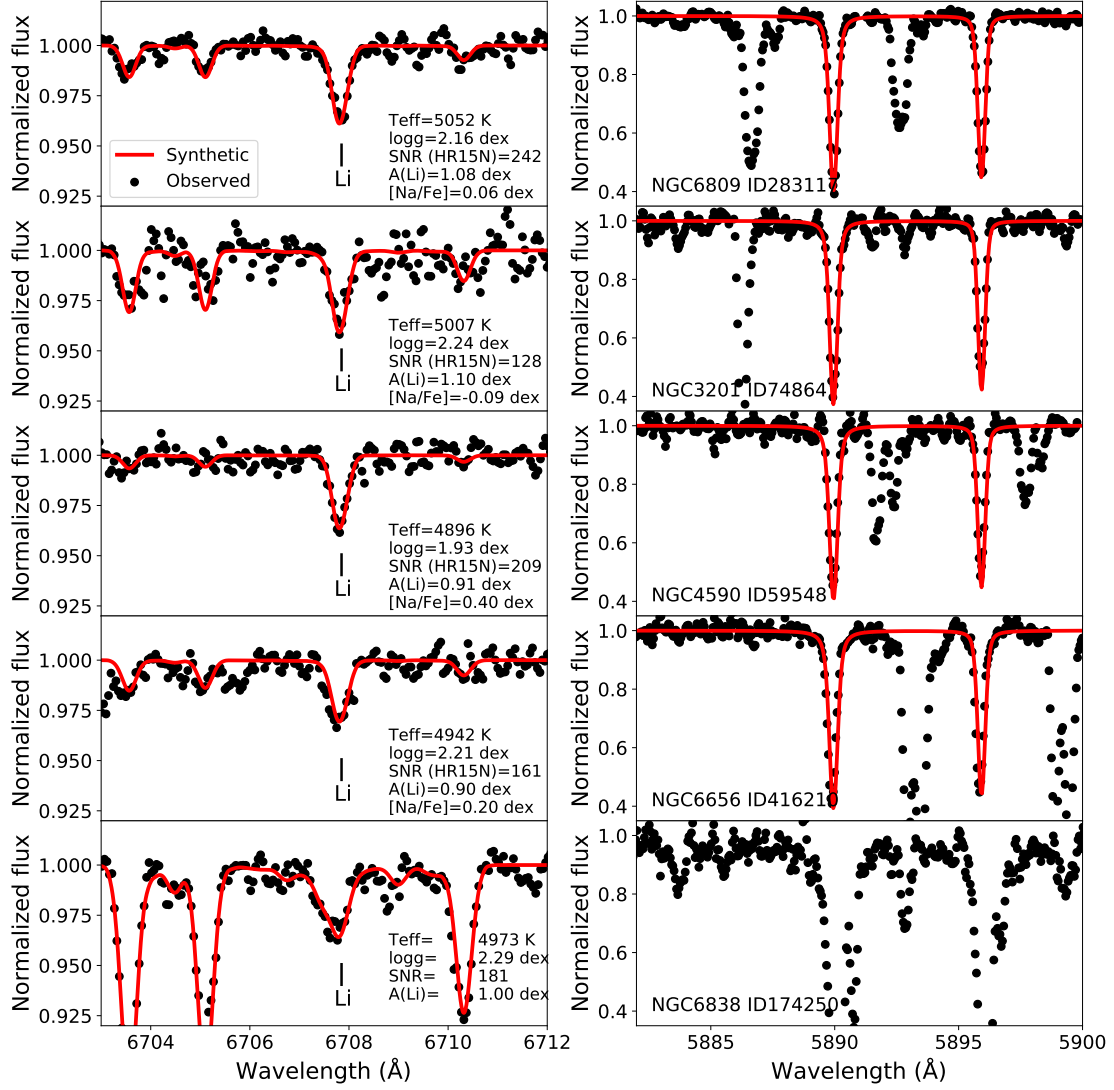


Fig. 1. Spectra from one typical sample star in each of the clusters in the region of the Li line (left) and the Na doublet (right), and the respective synthetic fits to the lines to measure the abundances. Stellar parameters, NLTE abundances, and S/N of the spectra are indicated for each star.

Table 2. Colour excess $E(B-V)$ and distance modulus for each cluster.

Cluster	$E(B-V)$	Source ^a	$(m - M)_0$ mag	Source ^b
NGC4590	0.06	SF11	15.00	K+15
NGC6809	0.12	SF11	13.95	VBD18
NGC6656*	0.33	S+98	13.60	H10
NGC3201*	0.24	B+13	14.20	H10
NGC6838	0.28	SF11	13.80	H10

Notes. Adopted colour excess $E(B-V)$ and distance modulus adopted for each cluster. Clusters marked with * were corrected by differential reddening.

^(a) SF11: Schlafly & Finkbeiner (2011); S+98: Schlegel et al. (1998); B+13: Bonatto et al. (2013).

^(b) VBD18: VandenBerg & Denissenkov (2018); K+15: Kains et al. (2015); H10: Harris (1996, 2010 edition).

by Harris (1996, 2010 edition) to prevent degeneracy. We build a probability distribution with all the isochrone points in a 3σ radius from the input parameters. This method was preferred to

measuring $\log g$ spectroscopically given the lack of a relevant number of Fe II lines in our spectra. Additionally, Mucciarelli & Bonifacio (2020) recommend to use photometric temperatures and gravities in low-metallicity stars of globular clusters, since spectroscopic parameters are lower than photometric determinations, and inconsistent with the position of the giants in color-magnitude diagrams.

We compared the calculated $\log g$ with $\log g$ estimated using bolometric luminosity of the giants and find a good agreement between both methods. Uncertainties obtained are $\Delta \log g \approx 0.2$ dex. As for the error in effective temperature, we adopt typical uncertainties of $\Delta T_{\text{eff}} \approx 125$ K, that correspond to the standard deviation of the colour relation used (Alonso et al. 1999).

Microturbulence velocities are then calculated for each star using their effective temperature, $\log g$, and the relation in Bruntt et al. (2012). The typical errors when using this relation are reported to be 0.13 km s^{-1} by the authors. However, this value depends on uncertainties in effective temperature and $\log g$, assumed to be 100 K and 0.1 dex respectively. Given that our uncertainties are slightly higher, we assume a typical error in microturbulence velocity of 0.15 km s^{-1} .

Table 3. Mean metallicity and number of members for each cluster.

Cluster	[Fe/H] dex	SD _[Fe/H] dex	Harris [Fe/H] dex	Members
-	-	-	-	-
NGC4590	-2.34	0.10	-2.23	46
NGC6809	-1.79	0.10	-1.94	90
NGC6656	-1.77	0.12	-1.70	98
NGC3201	-1.58	0.06	-1.59	83
NGC6838	-0.72	0.07	-0.78	32

Notes. Mean metallicity, standard deviation (SD), and number of members for each cluster. Metallicity values reported by Harris (1996, 2010 edition) are also included.

We calculated metallicities for each star individually by measuring the equivalent width of Fe I lines using the code DAOSPEC (Stetson & Pancino 2008) through the wrapper 4DAO⁴ (Mucciarelli 2013). Then, the Fe abundances were derived with the code GALA (Mucciarelli et al. 2013). Our Fe I line list was constructed by using the spectra of the coldest and hottest giants in the sample. We inspected visually the spectra to identify lines that were visible in both stars covering the entire effective temperature range. Although we considered initially a large list of lines, a spurious correlation between metallicity and effective temperature was identified in some of the clusters, with an extremely strong correlation in NGC3201. We only selected lines that did not saturate in any cluster, and as such were good indicators of the real metallicity of the star. Based on this test, we ended up selecting 6 lines with a linear correlation between equivalent widths and temperatures to only estimate the metallicity, and used it as an additional criteria of membership. We then calculated the mean metallicity of the sample and adopted that value for all stars of the cluster when we determine chemical abundances. We estimated the NLTE corrections for our selected Fe I lines, that could be relevant for metal-poor stars (Bergemann et al. 2012). Only two of the used lines have NLTE corrections reported by Mashonkina et al. (2016); in the temperature and log *g* ranges of NGC4590 stars, they amount to $\sim 0.072 - 0.085$ dex. These are the maximum values expected for our sample of stars, because NLTE corrections are larger for lower metallicities. We find no way to apply consistently Fe NLTE corrections, but these seem to be smaller than the reported uncertainty in metallicity, and would not affect significantly the measured abundances.

Table 3 shows the mean metallicity and final number of members in each cluster.

In NGC3201 we found some outliers in the metallicity distribution, which are likely non members, and were removed with sigma-clipping, using a criteria of 2σ . We aim for the maximum purity of the sample rather than completeness, and thus, although we might exclude some members, this procedure increases the probability of membership by selecting stars with metallicities closer to the mean of the cluster. Notice that while the mean metallicity of NGC3201 is similar in different literature sources, there is an ongoing debate about the existence of an intrinsic metallicity spread in the cluster (Alborno et al. 2021, and references therein). Given that we are selecting only stars with a metallicity similar to the mean of the cluster, the conclusion about the possible spread in the metallicity distribution should not change our results. The mean value of metallicity we obtain for NGC6809 is $[\text{Fe}/\text{H}] = -1.79 \pm 0.10$. The metallicity of this cluster seems to be controversial, with some measurements sim-

ilar to the value we report (e.g. Kayser et al. 2008), and others closer to the $[\text{Fe}/\text{H}] = -1.94$ value found in the Harris catalogue (e.g. Carretta et al. 2009a).

The final parameters for member stars in each of the 5 clusters can be found in Table A.1, in Appendix A.

4. Chemical abundances

4.1. Lithium

Lithium abundances are calculated using spectral synthesis around the Li doublet at wavelength ~ 6708 Å. The observed spectrum was compared to synthetic spectra generated using MOOG (Snedden 1973, 2018 version), with ATLAS9 model atmospheres (Castelli & Kurucz 2003) and the abundance derived through χ^2 minimization. The continuum level, one of the greatest uncertainties in the determination of Li abundance with this method, was set by using a region of ~ 10 Å around the Li line. For some of the giants where the Li line is not detected, only upper limits are reported. We estimated the detection limits on Li using the relation by Cayrel (1988) for the minimum equivalent width that could be measured in each spectra, and calculate the corresponding lithium abundance for 3 times that limiting equivalent width.

We calculated non local thermodynamical equilibrium (NLTE) corrections using the grid of Lind et al. (2009a). In NGC3201, NGC4590, and NGC6656, corrections are usually smaller than 0.1 dex, while in NGC6809 corrections are even smaller (< 0.06 dex). In contrast, NGC6838 has larger corrections, from 0.01 dex to 0.15 dex. Two stars in NGC4590 are outside the limits of the grid, and thus we use the closest grid point as the values for the Li correction.

The error in lithium is calculated by adding in quadrature the uncertainties associated to the synthetic spectra producing the best fit, something that depends greatly on the positioning of the continuum, and the propagation of errors in stellar parameters, in particular, of effective temperature that produces the largest deviations in $A(\text{Li})$. The typical uncertainties due to the quality of the data are of the order of $\Delta A(\text{Li}) \sim 0.05$ dex, which depends on the signal-to-noise ratio of the spectrum. This refers to uncertainties in the fitting procedure, including continuum placement and adjustments in the fit due to small changes in the radial velocity and line broadening. NGC3201 is the cluster with the overall worst quality spectra, and as such it can show higher errors of up to $\Delta A(\text{Li}) \sim 0.08$ dex. Uncertainties in the Li abundance arising from the propagation of errors in the stellar parameters are $0.10 - 0.17$ dex due to T_{eff} , $0.00 - 0.02$ dex due to the metallicity, and $0.01 - 0.03$ dex because of errors in log *g*. Errors propagated from microturbulence velocity (of ~ 0.01 dex) are added linearly, given that microturbulence velocity depends on effective temperature and log *g*. Our typical uncertainties are $\Delta A(\text{Li}) \simeq 0.16$ dex.

As a sanity check, we calculated the Li abundance in the cluster M4 using the same spectra used in Mucciarelli et al. (2011). The $A(\text{Li})$ we calculated using the same parameters as reported in that work is very similar for the RGB stars. We calculate an average difference $\langle \delta A(\text{Li}) \rangle = 0.09$. No attempt was made to reproduce the measurements in turn-off stars, as those are out of the scope of this paper. To check that our parameter determination was also consistent with previous literature, we also re-calculated stellar parameters from photometry directly, finding similar values and $A(\text{Li})$, with an average difference of $\langle \delta A(\text{Li}) \rangle = 0.16$.

⁴ <http://www.cosmic-lab.eu/4dao/4dao.php>

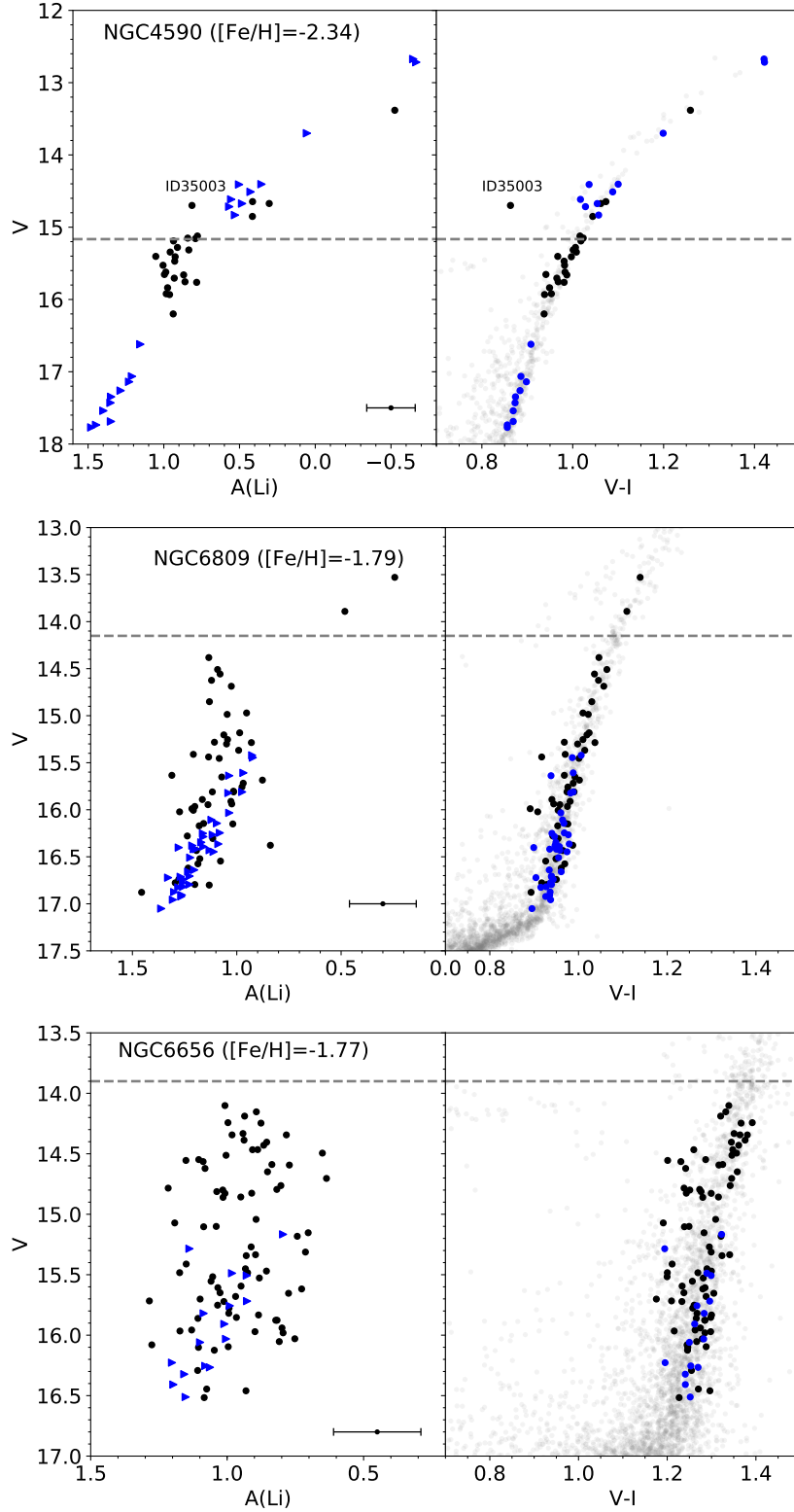


Fig. 2. Lithium abundances of NGC4590 (top panels), NGC6809 (middle panels), and NGC6656 (bottom panels) as a function of V magnitude (left panels) alongside their respective color-magnitude diagrams (right panels). Blue symbols are Li upper limits. The approximate position of the luminosity function bump in each cluster is marked with a dashed line.

4.2. Sodium

The sodium abundance was measured from the Na D doublet at 5890 – 5896 Å, also using spectral synthesis of the region, generating a grid of synthetic spectra using SPECTRUM (Gray

& Corbally 1994), with the same ATLAS9 model atmosphere. The choice of using one code over other was only done by convenience of our available wrappers and methods. However, we have tested to see the difference between abundances using the

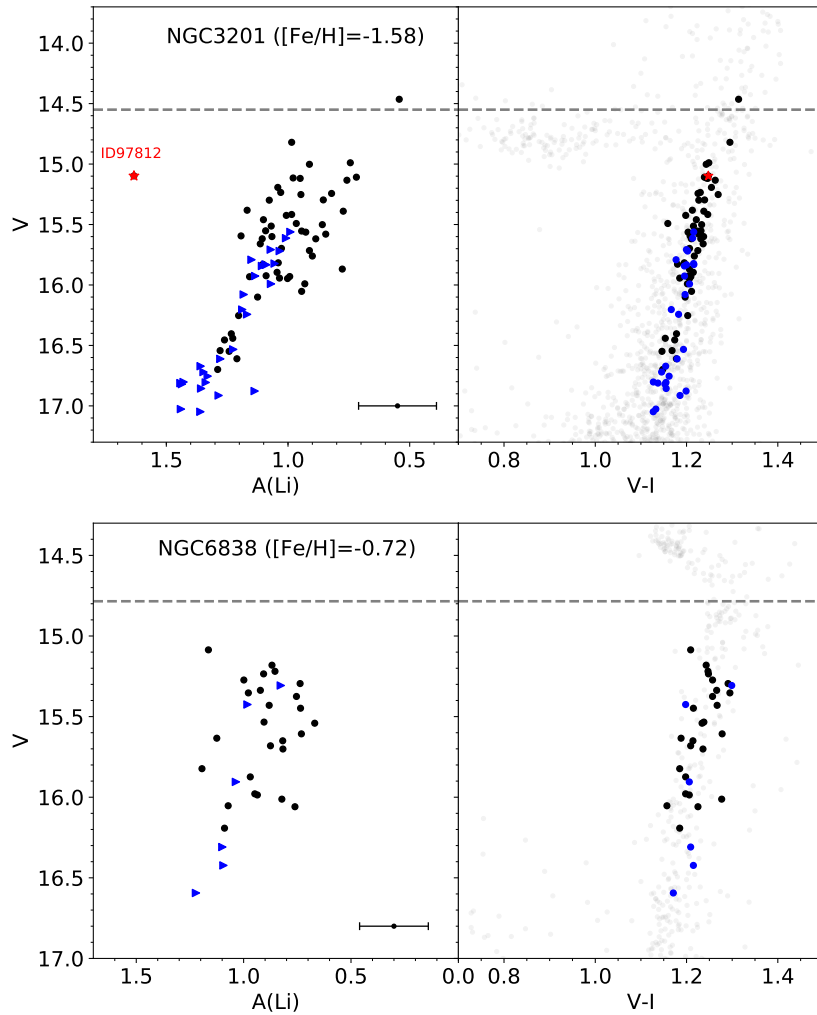


Fig. 3. Lithium abundances in NGC3201 (top panels) and NGC6838 (bottom panels) as a function of V magnitude (left panels), with their respective color-magnitude diagrams (right panels). Blue symbols are Li upper limits. The Li-rich red giant ID 97812 is marked as a red star. The dashed lines shows the position of the luminosity function bump.

two radiative transfer codes. Abundances of sodium change at most by 0.05 dex over the range of parameters of our sample. The best fit was selected with χ^2 minimization. The continuum placing is complicated by the low signal to noise of some of our spectra in the region. Accordingly, the errors in Na abundance consider these uncertainties. Uncertainties due to the continuum placement and quality of the fit can be as high as 0.10 dex. The propagation of errors in the stellar parameters gives typical Na uncertainties of ~ 0.11 dex due to T_{eff} , ~ 0.14 dex because of errors in $\log g$, ~ 0.01 dex uncertainty due to metallicity, and ~ 0.02 dex due to uncertainties in the microturbulence velocity. Typical uncertainties then are $\Delta A(\text{Na}) \approx 0.18$ dex.

We applied the Na NLTE corrections computed by Lind et al. (2011), that can be substantial for sodium measured from the D doublet, even reaching values of -0.5 dex within our sample.

It was not possible to measure sodium in NGC6838 due to the presence of contamination by interstellar sodium in that region of the spectra, close to the position of the stellar Na lines.

Typical spectra from our sample in the regions of the Li line and Na doublet is shown in Figure 1. These spectra show the quality of our data, and typical fits to the Li and Na lines to measure abundances. In the right panels, we also see the strong interstellar sodium lines.

5. Results

NLTE lithium and sodium abundances of the LRGB stars in the studied globular clusters are found in Table A.1, in Appendix A. We also include LTE abundances in the online data. We show our measured Li abundances as a function of V magnitude and the position of member stars in their color magnitude diagrams in Figures 2 and 3, left and right panels respectively. The magnitudes are also corrected by differential reddening in these figures. Lithium upper limits are shown as blue arrows. The position of the luminosity function bump (Samus et al. 1995; Ferraro et al. 1999) is indicated for each cluster as a dashed line, and the background corresponds to the catalog from Stetson et al. (2019), cleaned using membership probabilities by Vasiliev & Baumgardt (2021), but without corrections by differential reddening. Lithium upper limits in all five clusters are above our reported measurements, and as such are consistent with the abundances reported.

We first notice here that some of the stars show unusual positions in the color-magnitude diagram. This is because our initial selection of targets was not done using the Stetson photometry. We study each of these stars independently and follow them

throughout our analysis to make sure they are not contaminating our sample and confusing our results.

In NGC4590 the star ID35003 is not located in the locus of RGB stars of the cluster. This star has a proper motion, radial velocity, and metallicity consistent with NGC4590. We also check an independent measurement of its $\log g$ using bolometric corrections and find a very similar value between both determinations. However, given its color, this star has a higher temperature and higher lithium abundance ($A(\text{Li}) = 0.81$ dex) than other stars in the RGB of that magnitude. This star can be clearly identified in the left panel of Figure 2 with higher Li abundance. Thus, although consistent given our analysis, we consider that this star may not be part of the cluster due to its unusual position in the color-magnitude diagram and remove it from further analysis.

NGC6656 shows a broad RGB even after corrections by differential reddening. The bluer sequence does not show a particular spatial location, indicating that this is probably not the effect of additional differential reddening and that the broad sequence might be due to the spatial resolution of the used reddening maps. This cluster is suspected to have an intrinsic iron spread (Da Costa et al. 2009), but see also Mucciarelli et al. (2015).

In some of the clusters we can identify the position of the end of the FDU and the RGB bump in both panels, with abrupt decreases in $A(\text{Li})$. In NGC4590 we can clearly identify stars going through the FDU, diluting their Li at $V \sim 17$ mag, then a plateau formed by the LRGB and a second decrease in $A(\text{Li})$ produced by the inclusion of giants located after the luminosity function bump. Most of the upper RGB stars have only Li upper limits. Cluster NGC6809 has two stars after the RGB bump, while NGC3201 has only one, that shows a smaller Li abundance than the rest of RGB stars, at the level of the lower envelope of the Li distribution of LRGBs. We are able to identify the end of the FDU in NGC3201, where stars at the bottom of the RGB decrease their Li abundances. The Li dilution due to FDU in NGC6656 or NGC6838 is not clearly visible. In NGC6656, the abundance slowly decreases as we move up in the giant branch, with a large scatter, and the plateau is not as clear as in other clusters.

We also notice that there is a giant in NGC3201 (namely giant ID 97812, a red star symbol in Figure 3) with unusually high Li abundance $A(\text{Li})_{\text{NLTE}} = 1.63 \pm 0.18$ dex. Given that it is located before the onset of efficient extra-mixing, this Li-rich giant has probably experienced pollution from an external source. We analyze it further in Section 5.3.

5.1. LRGB plateau and the cosmic Li problem

To better identify a possible LRGB plateau in the 5 globular clusters we have binned the Li abundance as a function of effective temperature in Figures 4 and 5. Left panel shows the Li abundance as a function of effective temperature, where we include upper limits as blue arrows. The right panel shows the binned abundance as blue points but only considering Li measurements (gray points) and no upper limits. To select stars that belong to the plateau, we define the end of the first dredge-up by using the measured Li abundances. We perform a simple bilinear fit to the data in the $A(\text{Li})$ - T_{eff} diagram, from the highest temperature to the luminosity function bump, which is clearly signposted by the sharp drop of Li abundances with decreasing temperature. The fit provides the approximate temperature where the abundance plateau starts, whilst the luminosity function bump marks its end. Notice that in NGC4590 there are no stars that have completed the first dredge-up, as suggested by our fit to the data. We identify the bins that belong to the LRGB plateau as red squares,

which are the values we use to calculate the mean Li abundance of the plateau in each cluster. The stars are binned in equal-sized temperature ranges within each cluster, to make sure that there is a significant number of stars in each bin. Changing the bin size does not significantly alter our results.

The binned Li abundance allows to better identify the LRGB plateau present in the clusters. In NGC4590, the value of this plateau is $A(\text{Li}) = 0.90 \pm 0.08$ dex. The error reported here is the standard deviation of the individual abundances of stars at the plateau. NGC6809 shows a clear decrease in Li at the start of the RGB until reaching a plateau of $A(\text{Li}) = 1.03 \pm 0.08$ dex. The effect of the FDU can also be observed in NGC6656, where in this case, the LRGB reach a value of $A(\text{Li}) = 0.88 \pm 0.09$ dex. In NGC6838 we also identify a mean Li in LRGB stars of $A(\text{Li}) = 0.84 \pm 0.10$ dex. The only cluster where the LRGB do not have a constant value is in NGC3201. Here we observe a decrease in the abundance from higher to lower temperatures. The presence of a plateau is much harder to identify, and its value depends slightly on the position of the bins. If we define the plateau considering the 3 bins between ~ 4900 K to ~ 5050 K where the abundance seems to be constant, we find a mean abundance of $A(\text{Li}) = 0.97 \pm 0.10$ dex. Changing the bin size and position of bins, the mean $A(\text{Li})$ varies from 0.93 to 0.98 dex, with similar standard deviation. The main difference between this and other clusters in our sample is its age, but there is no clear explanation to the larger scatter near the plateau.

The scatter is fully consistent with the total error, which includes both the uncertainties due to quality of the spectra and uncertainties due to stellar parameters, especially effective temperature.

We use our Li abundances together with theoretical stellar evolutionary models to predict an initial Li value in these clusters. We use the Yale Rotating Evolutionary code (YREC, Pinsonneault et al. 1989; Demarque et al. 2008), without diffusion, rotation or overshooting. The models use mixing length theory for convection (Cox & Giuli 1968), which acts as the only mixing mechanism inside the star, with no extra-mixing to modify the surface abundances after the RGB bump. Additionally, we use 2006 OPAL equation of state (Rogers & Nayfonov 2002), and cross section for the proton capture by lithium from Lamia et al. (2012). Other input physics included in these standard models can be found in Aguilera-Gómez et al. (2016). For each of the clusters we run models with a mass $M = 0.8 M_{\odot}$, considered to be the typical turn-off mass in globular clusters, and a metallicity equal to the median value of the cluster, presented in Section 3.

The effects of diffusion, that can significantly change the lithium abundance in the main sequence evolutionary phase (Richard et al. 2002), are almost completely erased in the LRGB, given that the diffusion layers are mixed again by the deepening convective envelope. The lithium abundance in the LRGB of standard models is at most 0.07 dex higher than when models include diffusion (Mucciarelli et al. 2012).

Models with an initial lithium abundance equal to the standard BBN value of $A(\text{Li}) = 2.72$ dex produce LRGB Li values much larger than those observed. Instead, we attempt to find this primordial Li abundance. We modify the initial Li abundance of the models to match the Li in LRGB, post FDU dilution. These results can be seen in Figure 6. The model presented for the cluster NGC4590 has a metallicity of $[\text{Fe}/\text{H}] \sim -2.2$, which is the lowest metallicity we had available for the models. We tested that at such low metallicity the initial abundance should not change significantly between that metallicity and the metallicity measured for the cluster ($[\text{Fe}/\text{H}] = -2.34$ dex).

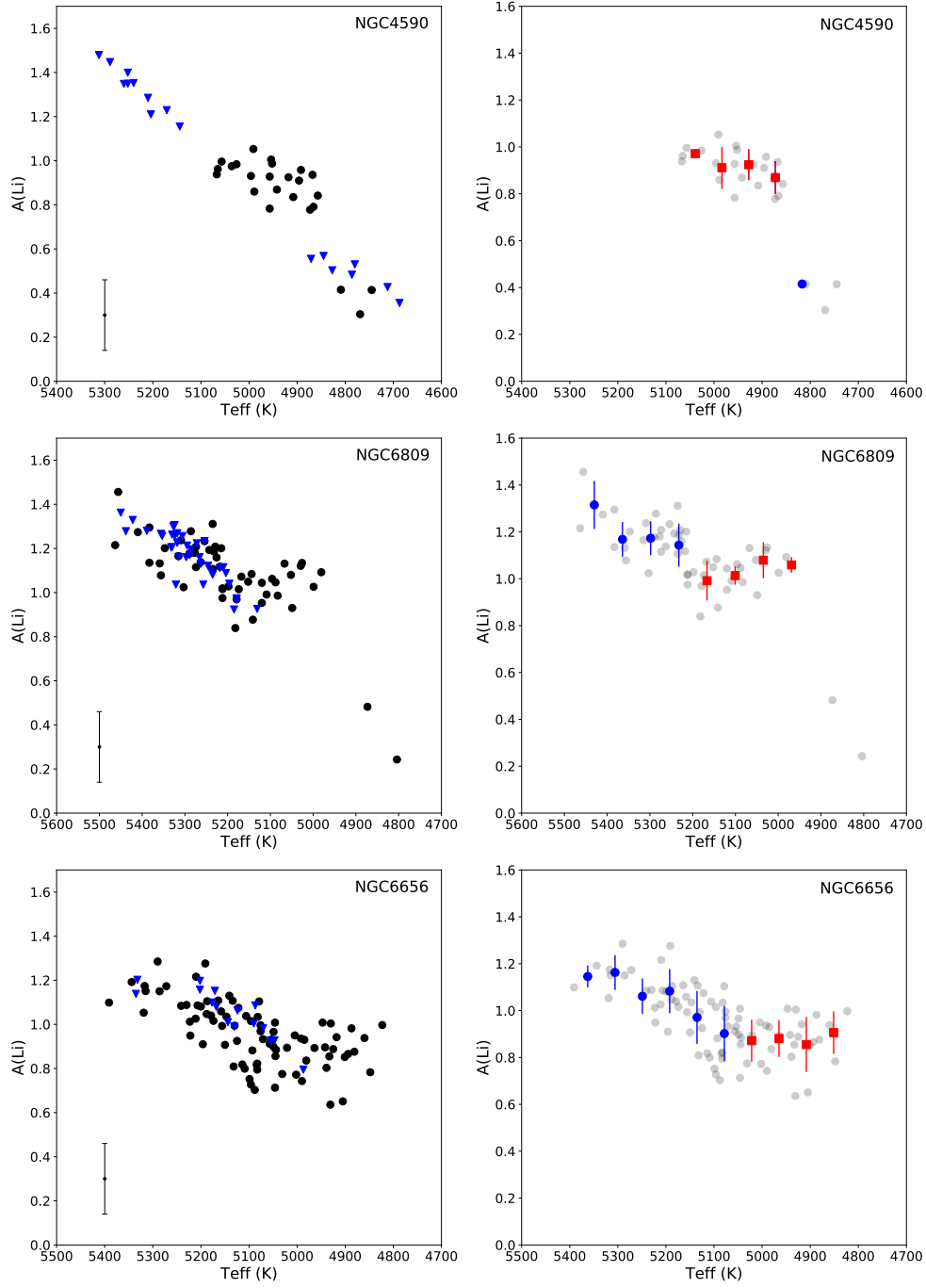


Fig. 4. Behavior of lithium abundances as a function of effective temperatures for NGC4590, NGC6809, and NGC6656, from top to bottom panels. The left panels show the abundances (black points) and upper limits (blue arrows). The right panels only show the measurements in gray and the binned Li abundances, considering equal-sized bins (blue points). Red squares mark the bins considered to be part of the Li LRGB plateau and used to calculate mean values reported.

Signatures of diffusion have been found in some globular clusters (e.g. Korn et al. 2006; Gruyters et al. 2016). The overall effect of diffusion in main sequence stars is to lower the surface Li abundance when approaching the turn-off, however observations suggest that the efficiency of diffusion is moderated by some competing mixing mechanism of unspecified origin. This makes it difficult to predict theoretically the Li abundance in turn-off stars of our studied clusters using the measured LRGB as starting point. Thus, we do not attempt to predict a turn-off abundance, and instead we recover the initial, primor-

dial Li abundances of these clusters with our models, considering that the effects of diffusion are erased during the FDU.

Predicted initial values in every case are very similar to the Spite plateau and $A(\text{Li})$ found in other globular clusters where the Li abundance can be measured in dwarfs. The inclusion of diffusion could decrease this predicted value by 0.07 dex at most. The primordial Li abundance of NGC6809 is predicted to be $A(\text{Li})_0 = 2.28$. We have also included here a model with $0.7 M_{\odot}$, to see the effects that mass can have in the abundance of dwarfs in the cluster. Li burning, including in the pre-main

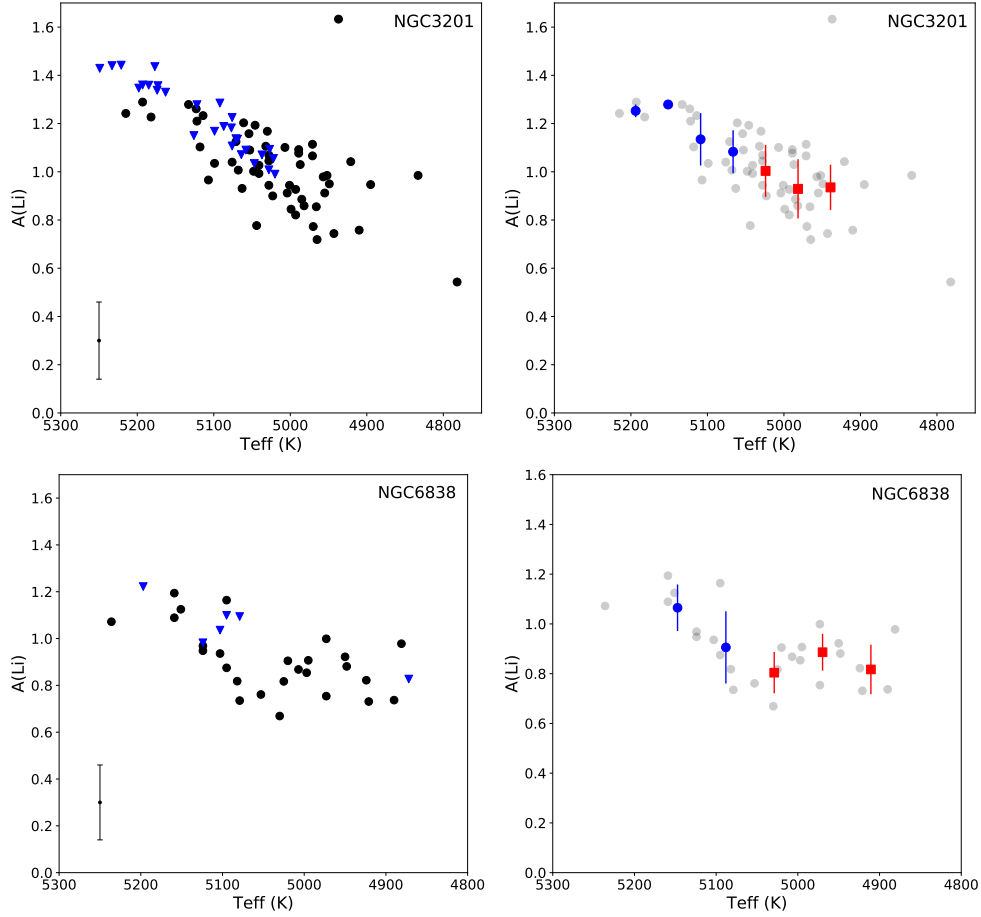


Fig. 5. Same as Figure 4 for NGC3201 (top panel) and NGC6838 (bottom panel).

sequence, can be substantially different in this mass range. By changing the mass of the model, and adjusting the Li in the LRGB, the predicted initial lithium changes by 0.08 dex, with a primordial value of $A(\text{Li})_0 = 2.20$, both within values found in halo stars. The initial lithium predictions of the other clusters are $A(\text{Li})_0 = 2.16$ in NGC4590, $A(\text{Li})_0 = 2.14$ for NGC6656, $A(\text{Li})_0 = 2.21$ in NGC3201, and $A(\text{Li})_0 = 2.17$ in NGC6838. These predicted primordial $A(\text{Li})$ values calculated for each cluster match the Li abundances of the Spite plateau and other globular clusters in the literature.

We report in Table 4 LRGB stars abundances of the studied clusters and others in the literature. We also report in this table our predicted initial Li abundances and the Li abundance in the turn-off of clusters where it has been measured. Notice here that measurements are not homogeneous, and temperature scales can change the Li abundance measurements. There does not seem to be any correlations between the Li abundance in the LRGB (or the predicted primordial value) and metallicity for different clusters (Figure 7).

The use of a different temperature scale could also change our Li measurements and estimated primordial abundances in the clusters. By using a hotter temperature scale (e.g., González Hernández & Bonifacio 2009), our Li abundances should be higher by ~ 0.1 dex. The use of different stellar evolutionary models, or even different prescriptions in the model used (e.g., including overshooting or changing the efficiency of diffusion) can also modify the predicted estimation of cosmological Li (Mucciarelli et al. 2012), and even make it higher than the Spite

Plateau, although differences in the temperature scale of those measurements should also be taken into account (e.g. Meléndez & Ramírez 2004). Thus, our predictions should not be considered as an attempt to precisely obtain the exact primordial lithium of each cluster, but rather an estimation of the possible abundance range.

5.2. First and second population stars

Measurements of the Na abundance were made in order to separate populations in the studied globular clusters. This is based on the idea that the more massive stars of the first population, now evolved, had an active nucleosynthesis cycle in its interior able to produce, for instance, fresh Na at the expense of O. Throughout the lifetime of the star, this processed material is carried to the surface of the star, and through mass loss, stellar winds, and the planetary nebula phase, to the interstellar medium. The second population of stars is born from this polluted material, creating different populations of stars coexisting in the same cluster (see e.g. Bastian & Lardo 2018). The nature of the polluter is still a matter of open debate, with fast rotating massive stars (Decressin et al. 2007) and asymptotic red giant branch stars (AGB, Ventura & D’Antona 2009) being the main contenders. On the other hand, there could be alternative scenarios to explain this pattern in clusters, not related to nucleosynthesis, or it is possible that the generational scenario is complicated by additional mechanisms acting (Gratton et al. 2019).

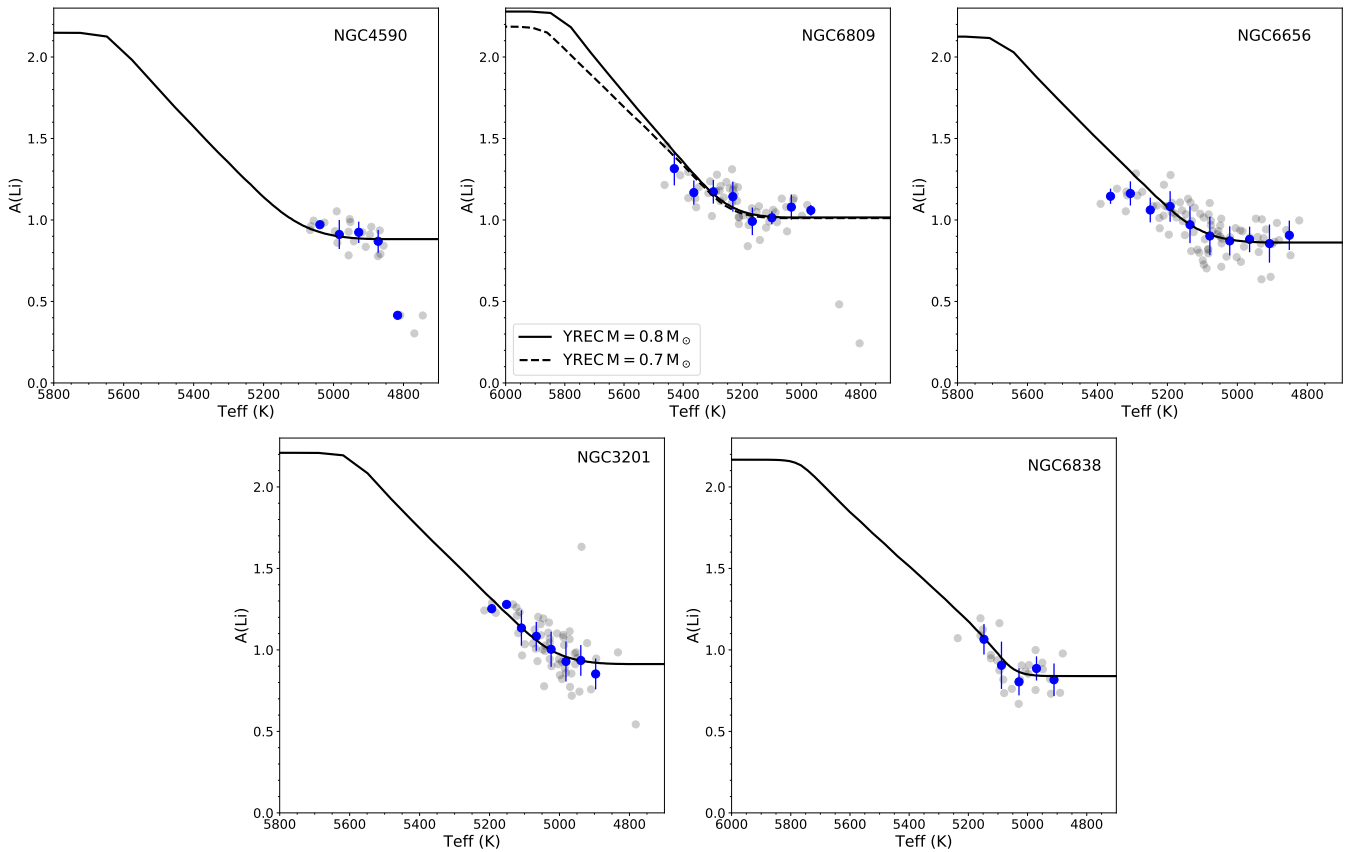


Fig. 6. Lithium abundance as a function of effective temperature. Blue points are the binned abundance in equal-sized bins. We include theoretical models that fit the LRGB Li plateau. In the cluster NGC6809, we include models with 0.7 and $0.8 M_{\odot}$.

Li, which is destroyed at relatively low temperatures by proton capture, is expected to be depleted in Na-enriched material, such as that from which second population stars are born. An anticorrelation between Na and Li is then expected. However, in certain AGB stars, Li can be created in the interior through the Cameron-Fowler mechanism (Cameron & Fowler 1971), and is quickly transported to the surface of the star by convection, where the cooler temperatures prevent it from destruction by proton capture (Sackmann & Boothroyd 1992). Thus, it may be relevant to compare the Li abundance from the first and second population, with the first population expected to have a cosmological Li content diluted because of the FDU, and the second population may show an abnormally high Li abundance if the polluter is either a Li-enriched AGB star or if the ejecta of polluters is mixed with material that has not burned Li.

Figures 8 and 9 show the behavior of $A(\text{Li})$ as a function of $[\text{Na}/\text{Fe}]$ only for RGB stars in NGC4590 and NGC6809 (top and bottom panels of Figure 8 respectively), and NGC6656 and NGC3201 (top and bottom panels of Figure 9). We have removed stars brighter than the RGB bump in these figures. Additionally, we consider only LRGB plateau stars in the right panel of these figures, by removing all stars that have not yet completed their first dredge-up. As mentioned in Section 4, we were not able to measure Na in NGC6838, thus we do not present results for that cluster. Focusing only on LRGB stars, there is no clear correlation between Li and Na in NGC4590, NGC6809, NGC3201, and NGC6656. We do see some star-to-star scatter, but Li does not scale with Na. This, however, does not exclude

the possibility to find a trend if more stars are considered in the analysis.

As previously mentioned, there is no statistically significant anticorrelation in NGC6656. By eye, when considering all RGB stars of different effective temperatures in the top left panel of Figure 9, objects with higher Na would seem to have slightly lower Li. However, when we look for possible correlations by binning both in effective temperature and Na, only the higher temperature bin shows a hint of an anticorrelation, that is however not considered statistically significant.

The lack of a clear Li-Na anticorrelation in our cluster sample needs further confirmation with additional data. In the literature, some clusters do show correlations between Li and other light element abundances. NGC6752 presents a Li-O correlation (Shen et al. 2010) and Li-Na anticorrelation (Pasquini et al. 2005). NGC6397 has some stars enriched in Na that are Li poor (Lind et al. 2009b). NGC2808 has some stars enriched in Al that are Li depleted (D’Orazi et al. 2015b). In M4 there is something like a Li-Na anticorrelation (Monaco et al. 2012) but no Li-O correlation (Mucciarelli et al. 2011). 47 Tuc shows no sign of a Li-Na anticorrelation (Dobrovolskas et al. 2014).

If it is confirmed that some clusters have a similar Li abundance in both populations, this would point to a higher Li than expected in the second population. This could mean that the birth material of these stars should have been mixed with relatively Li-rich material, pointing to AGB stars as possible polluters. Models have to be fine-tuned to produce such a pattern in globular clusters, given that the Li yields have great uncertainties depending on how physics such as mass loss is introduced (Ventura &

Table 4. Lithium abundance in the LRGB plateau and turn-off of galactic globular clusters.

Cluster	[Fe/H] (dex)	A(Li) _{LRGB} (dex)	A(Li) ₀ (dex)	Reference
-	-	-	-	-
NGC4590	-2.34	0.90 ± 0.08	2.16	This work
NGC6809	-1.79	1.03 ± 0.08	2.28	This work
NGC6656	-1.77	0.88 ± 0.09	2.14	This work
NGC3201	-1.58	0.97 ± 0.10	2.21	This work
NGC6838	-0.72	0.84 ± 0.10	2.17	This work
Cluster	[Fe/H]	A(Li) _{LRGB}	A(Li) _{TO}	Reference
NGC7099	-2.30	1.10 ± 0.06	2.21 ± 0.12	1 ^a
NGC6397	-2.10	1.13 ± 0.09	2.25 ± 0.01 ± 0.09	2 ^a
M4	-1.10	0.92 ± 0.01 ± 0.08	2.30 ± 0.02 ± 0.10	3 ^a
M4	-1.31	-	2.13 ± 0.09	4
NGC6752	-1.68	0.83 ± 0.15	-	5
NGC1904	-1.60	0.97 ± 0.02 ± 0.11	-	6
NGC2808	-1.14	1.06 ± 0.02 ± 0.13	-	6
NGC362	-1.26	1.02 ± 0.01 ± 0.11	-	6
NGC6218	-1.37	1.07 ± 0.01 ± 0.06	-	7
NGC5904	-1.29	1.02 ± 0.01 ± 0.11	-	7
47 Tuc	-0.76	-	1.78 ± 0.18	8
M92	-2.00	-	2.36 ± 0.19	9
ω Cen	-1.50	-	2.19 ± 0.14	10

References. (1) Gruyters et al. (2016); (2) Lind et al. (2009b); (3) Mucciarelli et al. (2011); (4) Monaco et al. (2012); (5) Mucciarelli et al. (2012); (6) D’Orazi et al. (2015b); (7) D’Orazi et al. (2014); (8) Dobrovolskas et al. (2014); (9) Bonifacio (2002); (10) Monaco et al. (2010)

Notes. ^(a) These works present Li abundances in the turn-off and lower red giant branch.

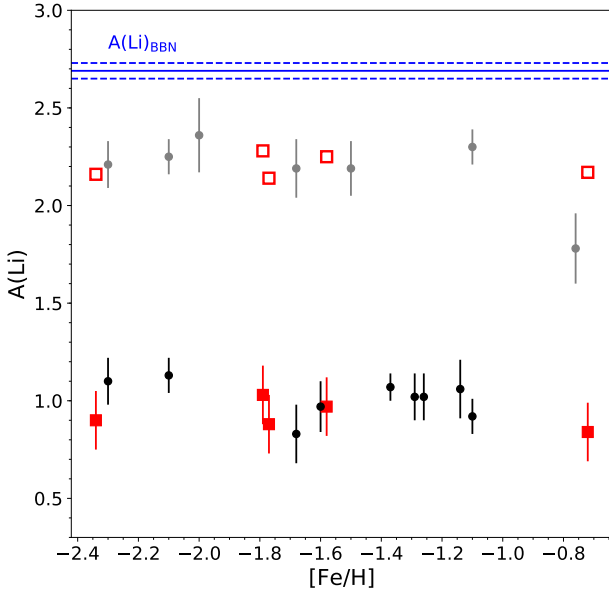


Fig. 7. Li abundance in the LRGB of the 5 studied globular clusters as a function of [Fe/H] (filled red squares). The calculated primordial abundances for these clusters are the empty red squares. These are compared to literature measurements of the lithium abundance in the LRGB (black points at low Li abundances) and in the turn-off stars (grey points at high Li abundances) of globular clusters in the Galaxy. Also the Big Bang Nucleosynthesis prediction from Coc et al. (2014) is included and shown as a blue line, with the dashed blue lines representing its reported uncertainties.

D’Antona 2010). If massive stars were the polluter, this scenario would require mixing the Na-rich material from the ejecta with unprocessed material that has a higher Li abundance. However,

confirmation of the lack of a Na-Li anticorrelation is needed before anything can be firmly concluded about the mechanism behind the different populations in clusters. Additionally, measurements from clusters come from non-homogeneous sources that not only have different parameters scales, spectral qualities, and use different methods, but that also provide abundances of different light elements. An homogeneous determination of properties and abundances could be a major improvement to gain insight about the second generation polluters.

5.3. Li-rich giant in NGC3201

Stars in the red giant branch experience abundance changes during the FDU, and then, at the luminosity function bump where the extra-mixing acts. If a solar-like star enters the RGB phase with a meteoritic abundance $A(\text{Li}) = 3.3$, its predicted Li abundance after the FDU is expected to be $A(\text{Li}) = 1.5$, only considering FDU dilution. However, values can be much lower, when additional ingredients, such as a much lower initial Li abundance, Li burning, and main sequence mixing are taken into account. The precise value to classify a giant as enriched is actually mass and metallicity dependent, and standard giants with higher $A(\text{Li})$ than 1.5 dex can be found, as well as giants with lower abundances that could have experienced a Li-enrichment process (Aguilera-Gómez et al. 2016). In spite of predictions from canonical models, lithium-rich red giants, with higher Li abundances, even reaching or exceeding the meteoritic value, are known to exist (e.g. Wallerstein & Sneden 1982; Monaco et al. 2011).

Globular clusters present an advantage, with all of their giants sharing a similar mass, and possibly, a similar original Li content. Because of this, we can compare the Li abundance of the giants to abundances of other stars with similar parameters and at a similar evolutionary stage, making enriched objects much easier to identify. Although Li-rich giants are unusual in gen-

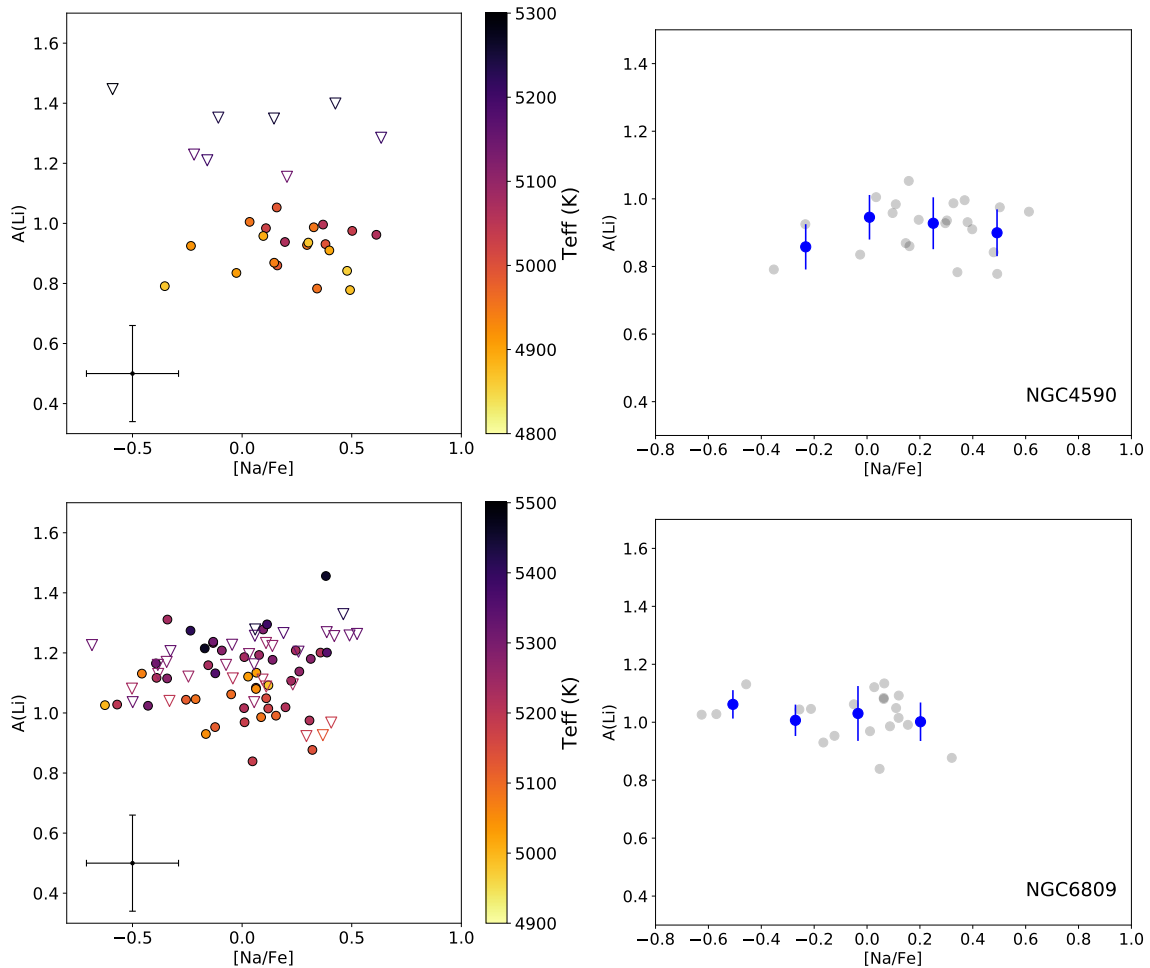


Fig. 8. Lithium abundance as a function of sodium abundance. The left panel is color-coded by effective temperature, and includes all RGB stars before the luminosity function bump, while the right panel considers only Li measurements (no upper-limits) of plateau LRGB stars, and it is binned (blue points) to show possible trends between both abundances. Top panel is NGC4590, bottom panel shows NGC6809.

eral, they are particularly rare in globular clusters. Only about a dozen giants are known to have a much higher Li abundance than other stars in the same evolutionary stage in a globular cluster. So far, Li enriched RGB stars have been found in NGC5272 (Kraft et al. 1999), NGC362 (Smith et al. 1999; D’Orazi et al. 2015a), NGC4590 (Ruchti et al. 2011; Kirby et al. 2016), NGC5053, NGC5897 (Kirby et al. 2016), 2 giants in NGC7099 (Kirby et al. 2016), ω Cen (Mucciarelli et al. 2019), and only one Li-rich star in NGC1261 (Sanna et al. 2020).

These are located all along the RGB phase, although AGB Li-rich stars have also been found (e.g. Kirby et al. 2016). Some are located after the luminosity function bump of their respective clusters, where extra-mixing is expected to affect the abundance of stars and could be the reason behind the Li-enrichment. Before that point in evolution, other explanations must be invoked that require pollution from an external source or the presence of a binary companion to trigger Li production (Casey et al. 2019). In the case of pollution, the source could be an AGB companion that can produce additional lithium in its interior and could then be transferring mass to the RGB star; it could be a nova, that can produce Li during the thermonuclear runaway (Starrfield et al. 1978; Izzo et al. 2015); or a planet or brown dwarf accreted by the star, objects that preserve the Li they have at formation (Alexander 1967; Siess & Livio 1999).

We present the discovery here of one more Li-rich giant in a globular cluster, in this case, NGC3201. The star ID 97812, with $A(\text{Li})_{\text{NLTE}} = 1.63 \pm 0.18$ dex is located before the luminosity function bump, and thus it is not expected to be enriched by the internal production of Li. Instead, pollution, either during the RGB phase or before, is probably the cause of enrichment for this giant, it is still possible that the presence of a binary companion is triggering the Li enhancement. Considering accretion as a possible scenario, we calculate the Li abundance of the star after the engulfment of a planet, using the models and parameters from Aguilera-Gómez et al. (2016). Applying as initial conditions the Li abundance of the rest of the cluster, we calculate the engulfed mass of a hypothetical planet needed to explain the high $A(\text{Li})$ of this star. This model is shown in Figure 10. For Jupiter-like composition, a mass of $M_{\text{planet}} = 10.1 M_{\text{Jupiter}} = 1.92 \times 10^{31}$ g is needed, and if the engulfed object had an Earth-like composition, it would require a mass of $M_{\text{planet}} = 120 M_{\text{Earth}} = 7.17 \times 10^{29}$ g. Although the amount of Earth masses needed is large, the mass of the Jupiter-like planet required is in range of masses of exoplanets known that can orbit close to their parent star. Monitoring the radial velocity of this star would be interesting to understand if its enhancement comes from planet engulfment, or if a binary companion is responsible for its high Li abundance.

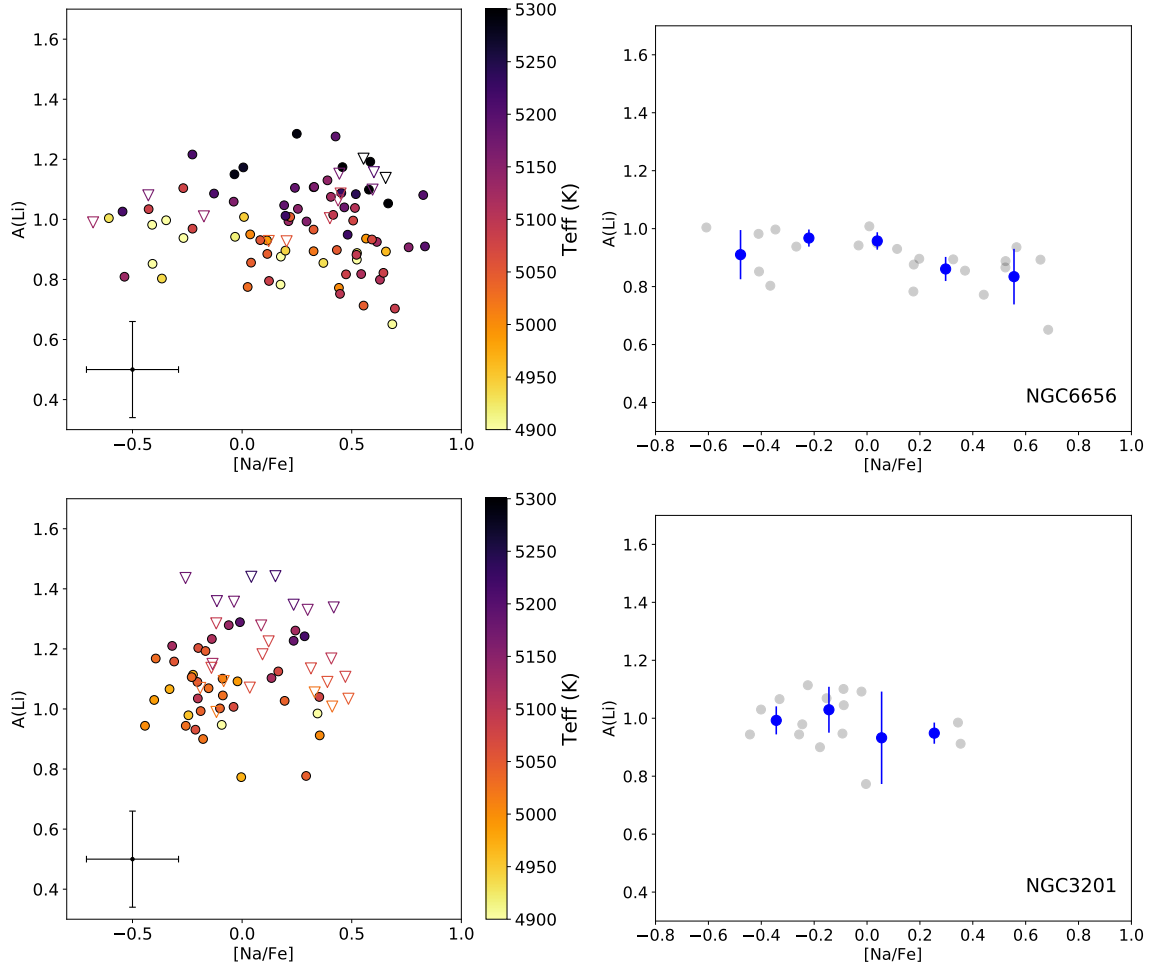


Fig. 9. Same as Figure 8. Top panels are NGC6656 and bottom panels NGC3201.

6. Summary

We calculated stellar parameters and measured Li and Na abundances of LRGB stars of 5 Galactic globular clusters, covering a wide range of metallicities from $[\text{Fe}/\text{H}] = -0.72$ to $[\text{Fe}/\text{H}] = -2.34$ dex. We find a LRGB plateau in all of the clusters at different levels, all between $A(\text{Li}) = 0.84 - 1.03$ dex, consistent with what has been found for other globular clusters previously.

Using theoretical models, we calculate the initial, primordial Li abundance in these clusters. The abundances found are similar to the Spite plateau value of halo stars, with $A(\text{Li}) = 2.14 - 2.28$. However, we note that the exact predicted value could change by using either a different temperature scale or different model. Thus, we use these predictions to conclude about the overall trends in Li abundances and not the exact value of the cosmological Li. As a caveat, we have to consider the possibility that the additional mixing operating during the main sequence which affects the efficiency of diffusion, might cause the transport of some extra Li in the burning regions (e.g. Richard et al. 2005). This would result in an underestimate of the initial $A(\text{Li})$ from measurements of LRGB using standard stellar models.

Considering the uncertainties in Li abundances, our main conclusion is that all of the clusters are consistent with models that have evolved from the same initial Li abundance. This agrees with the idea of a constant Li abundance of stars at this metallicity range, confirming the large discrepancy between Big

Bang Nucleosynthesis predictions and observations of main sequence field stars.

We find no correlation between the Li value in the LRGB plateau and metallicity. To further study a possible correlation, we also use literature data available for other clusters, finding no relation between $A(\text{Li})$ and $[\text{Fe}/\text{H}]$.

The measured sodium abundance is used to distinguish between first and second populations in each cluster. We find no clear difference in Li abundance between Na-rich and Na-poor stars in any of the clusters. If this is confirmed, it could point towards a class of polluter stars that are able to produce Li, such as AGB stars, or the mixing of the processed Li-poor medium with additional unprocessed matter.

We summarize the main results for each of the studied clusters:

- **NGC4590:** The median Li of LRGB stars in this metal-poor cluster is $A(\text{Li}) = 0.90 \pm 0.08$ dex. Considering its metallicity of $[\text{Fe}/\text{H}] = -2.34 \pm 0.10$ dex, we calculate an initial Li abundance $A(\text{Li})_0 = 2.16$. There is no clear correlation between Na and Li in this cluster when we only consider LRGB stars.
- **NGC6809:** The distribution of LRGB Li abundances in the cluster presents a peak at $A(\text{Li}) = 1.03 \pm 0.08$ dex. The primordial value predicted, considering a RGB mass of $0.8 M_\odot$ is $A(\text{Li})_0 = 2.28$. This is the cluster with the highest Li abundances in the LRGB plateau in our sample. It does not present a Li-Na correlation either.

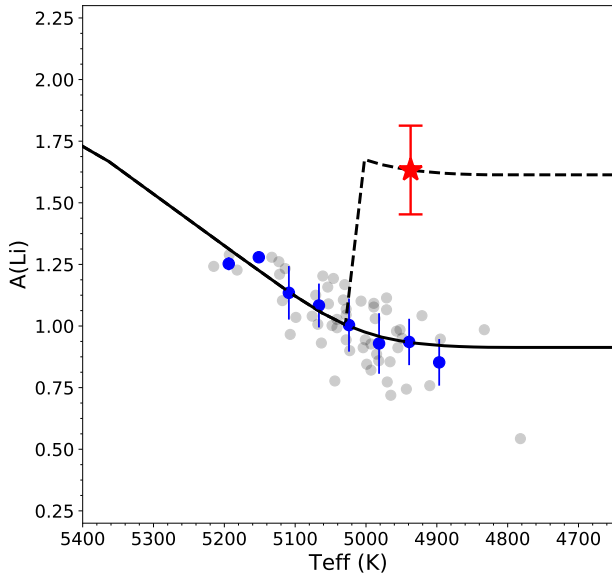


Fig. 10. Lithium abundance pattern of NGC3201. The Li-rich giant found (red star) could be explained by a model with planet engulfment (dashed line), where the hypothetical planet has a mass of $M_{\text{planet}} = 9.3 M_{\text{Jupiter}}$ (with Jupiter-like composition) or $M_{\text{planet}} = 110 M_{\text{Earth}}$ with Earth-like composition.

- **NGC6656:** In this cluster, the LRGB plateau is located at $A(\text{Li}) = 0.88 \pm 0.09$ dex, with a predicted initial value of $A(\text{Li})_0 = 2.14$.
- **NGC3201:** The RGB Li plateau is harder to identify in the cluster, as there appears to always be a small decrease in the abundance at decreasing temperatures. Considering this, we can define the LRGB stars between ~ 4900 K and ~ 5050 K and find a median abundance of $A(\text{Li}) = 0.97 \pm 0.10$ dex. Calibrating models to that value we find an initial $A(\text{Li})_0 = 2.21$. There is a Li-rich giant in this cluster with $A(\text{Li}) = 1.63 \pm 0.18$ dex, located before the luminosity function bump. Its evolutionary state indicated that its high Li abundance might be the product of external pollution and possibly, an accreted planet.
- **NGC6838:** Although the number of stars in this cluster is small, we are able to find a Li plateau value of $A(\text{Li}) = 0.84 \pm 0.10$ dex. This implies a primordial $A(\text{Li})_0 = 2.17$. Being the most metal-rich cluster in our sample, with $[\text{Fe}/\text{H}] = -0.72 \pm 0.07$ dex, we can compare its abundances with 47 Tuc. The similar LRGB Li abundance of NGC6838 with other clusters of lower metallicities suggests that, if all higher metallicity globular clusters experience main sequence depletion similar to 47 Tuc, the effect is mostly erased when they evolve to the RGB phase. It is also possible that 47 Tuc is a peculiar case of main sequence depletion. More abundance measurements of clusters at this high metallicity are needed to understand if either NGC6838 or 47 Tuc are unusual when compared to similar clusters.

Acknowledgements. We would like to thank the anonymous referee for their careful reading of the manuscript and helpful comments and suggestions. C.A.G. acknowledges support from the National Agency for Research and Development (ANID) FONDECYT Postdoctoral Fellowship 2018 Project number 3180668. This research was supported in part by the National Science Foundation under Grant No. PHY-1430152 (JINA Center for the Evolution of the Elements).

References

- Aguado, D. S., González Hernández, J. I., Allende Prieto, C., & Rebolo, R. 2019, *ApJ*, 874, L21
- Aguilera-Gómez, C., Chanamé, J., Pinsonneault, M. H., & Carlberg, J. K. 2016, *ApJ*, 829, 127
- Albornoz, Á. L., Villanova, S., Cortés, C. C., Ahumada, J. A., & Parisi, C. 2021, *AJ*, 161, 76
- Alexander, J. B. 1967, *The Observatory*, 87, 238
- Alonso, A., Arribas, S., & Martínez-Roger, C. 1999, *A&AS*, 140, 261
- Alonso-García, J., Mateo, M., Sen, B., et al. 2012, *AJ*, 143, 70
- Bastian, N. & Lardo, C. 2018, *ARA&A*, 56, 83
- Bergemann, M., Lind, K., Collet, R., Magic, Z., & Asplund, M. 2012, *MNRAS*, 427, 27
- Bessell, M. S. 1983, *PASP*, 95, 480
- Bonatto, C., Campos, F., & Kepler, S. O. 2013, *MNRAS*, 435, 263
- Bonifacio, P. 2002, *A&A*, 395, 515
- Bonifacio, P., Caffau, E., Spite, M., et al. 2018, *A&A*, 612, A65
- Bruntt, H., Basu, S., Smalley, B., et al. 2012, *MNRAS*, 423, 122
- Cameron, A. G. W. & Fowler, W. A. 1971, *ApJ*, 164, 111
- Carretta, E., Bragaglia, A., Gratton, R., D’Orazi, V., & Lucatello, S. 2009a, *A&A*, 508, 695
- Carretta, E., Bragaglia, A., Gratton, R., & Lucatello, S. 2009b, *A&A*, 505, 139
- Carretta, E., Bragaglia, A., Gratton, R. G., et al. 2009c, *A&A*, 505, 117
- Casey, A. R., Ho, A. Y. Q., Ness, M., et al. 2019, *ApJ*, 880, 125
- Castelli, F. & Kurucz, R. L. 2003, in *Modelling of Stellar Atmospheres*, ed. N. Piskunov, W. W. Weiss, & D. F. Gray, Vol. 210, A20
- Cayrel, R. 1988, in *The Impact of Very High S/N Spectroscopy on Stellar Physics*, ed. G. Cayrel de Strobel & M. Spite, Vol. 132, 345
- Chanamé, J., Pinsonneault, M., & Terndrup, D. M. 2005, *ApJ*, 631, 540
- Charbonnel, C. & Primas, F. 2005, *A&A*, 442, 961
- Choi, J., Dotter, A., Conroy, C., et al. 2016, *ApJ*, 823, 102
- Coc, A., Uzan, J.-P., & Vangioni, E. 2014, *J. Cosmology Astropart. Phys.*, 2014, 050
- Coelho, P., Barbuy, B., Meléndez, J., Schiavon, R. P., & Castilho, B. V. 2005, *A&A*, 443, 735
- Cox, J. P. & Giuli, R. T. 1968, *Principles of stellar structure*
- Da Costa, G. S., Held, E. V., Saviane, I., & Gullieuszik, M. 2009, *ApJ*, 705, 1481
- De Angelis, F., Piotto, G., Cassisi, S., et al. 2005, *AJ*, 130, 116
- Decressin, T., Meynet, G., Charbonnel, C., Prantzos, N., & Ekström, S. 2007, *A&A*, 464, 1029
- Demarque, P., Guenther, D. B., Li, L. H., Mazumdar, A., & Straka, C. W. 2008, *Ap&SS*, 316, 31
- Denissenkov, P. A. & Vandenberg, D. A. 2003, *ApJ*, 593, 509
- Dobrovolskas, V., Kučinskas, A., Bonifacio, P., et al. 2014, *A&A*, 565, A121
- D’Orazi, V., Angelou, G. C., Gratton, R. G., et al. 2014, *ApJ*, 791, 39
- D’Orazi, V., Gratton, R. G., Angelou, G. C., et al. 2015a, *ApJ*, 801, L32
- D’Orazi, V., Gratton, R. G., Angelou, G. C., et al. 2015b, *MNRAS*, 449, 4038
- D’Orazi, V., Lucatello, S., Gratton, R., et al. 2010, *ApJ*, 713, L1
- Dotter, A. 2016, *ApJS*, 222, 8
- Ferraro, F. R., Messineo, M., Fusi Pecci, F., et al. 1999, *AJ*, 118, 1738
- Fields, B. D. 2011, *Annual Review of Nuclear and Particle Science*, 61, 47
- Fu, X., Bressan, A., Molaro, P., & Marigo, P. 2015, *MNRAS*, 452, 3256
- Gaia Collaboration, Brown, A. G. A., Vallenari, A., et al. 2018, *A&A*, 616, A1
- González Hernández, J. I. & Bonifacio, P. 2009, *A&A*, 497, 497
- González Hernández, J. I., Bonifacio, P., Caffau, E., et al. 2009, *A&A*, 505, L13
- Gratton, R., Bragaglia, A., Carretta, E., et al. 2019, *A&A Rev.*, 27, 8
- Gratton, R. G., Sneden, C., Carretta, E., & Bragaglia, A. 2000, *A&A*, 354, 169
- Gray, R. O. & Corbally, C. J. 1994, *AJ*, 107, 742
- Gruyters, P., Lind, K., Richard, O., et al. 2016, *A&A*, 589, A61
- Harris, W. E. 1996, *AJ*, 112, 1487
- Hinshaw, G., Larson, D., Komatsu, E., et al. 2013, *ApJS*, 208, 19
- Izzo, L., Della Valle, M., Mason, E., et al. 2015, *ApJ*, 808, L14
- Kains, N., Arellano Ferro, A., Figueroa Jaimes, R., et al. 2015, *A&A*, 578, A128
- Kayser, A., Hilker, M., Grebel, E. K., & Willemsen, P. G. 2008, *A&A*, 486, 437
- Kirby, E. N., Guhathakurta, P., Zhang, A. J., et al. 2016, *ApJ*, 819, 135
- Korn, A. J., Grundahl, F., Richard, O., et al. 2006, *Nature*, 442, 657
- Kraft, R. P., Peterson, R. C., Guhathakurta, P., et al. 1999, *ApJ*, 518, L53
- Lamia, L., Spitaleri, C., La Cognata, M., Palmerini, S., & Pizzone, R. G. 2012, *A&A*, 541, A158
- Lee, Y. W., Joo, J. M., Sohn, Y. J., et al. 1999, *Nature*, 402, 55
- Lind, K., Asplund, M., & Barklem, P. S. 2009a, *A&A*, 503, 541
- Lind, K., Asplund, M., Barklem, P. S., & Belyaev, A. K. 2011, *A&A*, 528, A103
- Lind, K., Primas, F., Charbonnel, C., Grundahl, F., & Asplund, M. 2009b, *A&A*, 503, 545
- Marín-Franch, A., Aparicio, A., Piotto, G., et al. 2009, *ApJ*, 694, 1498
- Mashonkina, L. I., Sitnova, T. N., & Pakhomov, Y. V. 2016, *Astronomy Letters*, 42, 606
- McCall, M. L. 2004, *AJ*, 128, 2144

- Meléndez, J., Casagrande, L., Ramírez, I., Asplund, M., & Schuster, W. J. 2010, A&A, 515, L3
- Meléndez, J. & Ramírez, I. 2004, ApJ, 615, L33
- Molaro, P., Cescutti, G., & Fu, X. 2020, MNRAS, 496, 2902
- Monaco, L., Bonifacio, P., Sbordone, L., Villanova, S., & Pancino, E. 2010, A&A, 519, L3
- Monaco, L., Villanova, S., Bonifacio, P., et al. 2012, A&A, 539, A157
- Monaco, L., Villanova, S., Moni Bidin, C., et al. 2011, A&A, 529, A90
- Mucciarelli, A. 2013, arXiv e-prints, arXiv:1311.1403
- Mucciarelli, A. & Bonifacio, P. 2020, A&A, 640, A87
- Mucciarelli, A., Lapenna, E., Massari, D., et al. 2015, ApJ, 809, 128
- Mucciarelli, A., Monaco, L., Bonifacio, P., et al. 2019, A&A, 623, A55
- Mucciarelli, A., Pancino, E., Lovisi, L., Ferraro, F. R., & Lapenna, E. 2013, ApJ, 766, 78
- Mucciarelli, A., Salaris, M., & Bonifacio, P. 2012, MNRAS, 419, 2195
- Mucciarelli, A., Salaris, M., Bonifacio, P., Monaco, L., & Villanova, S. 2014, MNRAS, 444, 1812
- Mucciarelli, A., Salaris, M., Lovisi, L., et al. 2011, MNRAS, 412, 81
- Mucciarelli, A., Salaris, M., Monaco, L., et al. 2018, A&A, 618, A134
- Pancino, E., Ferraro, F. R., Bellazzini, M., Piotto, G., & Zoccali, M. 2000, ApJ, 534, L83
- Pasquini, L., Avila, G., Blecha, A., et al. 2002, The Messenger, 110, 1
- Pasquini, L., Bonifacio, P., Molaro, P., et al. 2005, A&A, 441, 549
- Pinsonneault, M. H., Kawaler, S. D., Sofia, S., & Demarque, P. 1989, ApJ, 338, 424
- Planck Collaboration, Ade, P. A. R., Aghanim, N., et al. 2014, A&A, 571, A16
- Prantzos, N. 2012, A&A, 542, A67
- Richard, O., Michaud, G., & Richer, J. 2002, ApJ, 580, 1100
- Richard, O., Michaud, G., & Richer, J. 2005, ApJ, 619, 538
- Rogers, F. J. & Nayfonov, A. 2002, ApJ, 576, 1064
- Ruchti, G. R., Fulbright, J. P., Wyse, R. F. G., et al. 2011, ApJ, 743, 107
- Sackmann, I. J. & Boothroyd, A. I. 1992, ApJ, 392, L71
- Samus, N., Kravtsov, V., Pavlov, M., Alcaïno, G., & Liller, W. 1995, A&AS, 109, 487
- Sanna, N., Franciosini, E., Pancino, E., et al. 2020, A&A, 639, L2
- Sbordone, L., Bonifacio, P., Caffau, E., et al. 2010, A&A, 522, A26
- Schlafly, E. F. & Finkbeiner, D. P. 2011, ApJ, 737, 103
- Schlegel, D. J., Finkbeiner, D. P., & Davis, M. 1998, ApJ, 500, 525
- Shen, Z. X., Bonifacio, P., Pasquini, L., & Zaggia, S. 2010, A&A, 524, L2
- Siess, L. & Livio, M. 1999, MNRAS, 308, 1133
- Simpson, J. D., Martell, S. L., Buder, S., et al. 2021, MNRAS, 507, 43
- Smith, V. V., Shetrone, M. D., & Keane, M. J. 1999, ApJ, 516, L73
- Snedden, C. A. 1973, PhD thesis, THE UNIVERSITY OF TEXAS AT AUSTIN.
- Spite, F. & Spite, M. 1982a, A&A, 115, 357
- Spite, M. & Spite, F. 1982b, Nature, 297, 483
- Starrfield, S., Truran, J. W., Sparks, W. M., & Arnould, M. 1978, ApJ, 222, 600
- Stetson, P. B. & Pancino, E. 2008, PASP, 120, 1332
- Stetson, P. B., Pancino, E., Zocchi, A., Sanna, N., & Monelli, M. 2019, MNRAS, 485, 3042
- Tonry, J. & Davis, M. 1979, AJ, 84, 1511
- VandenBerg, D. A. & Denissenkov, P. A. 2018, ApJ, 862, 72
- Vasiliev, E. & Baumgardt, H. 2021, MNRAS, 505, 5978
- Ventura, P. & D’Antona, F. 2009, A&A, 499, 835
- Ventura, P. & D’Antona, F. 2010, MNRAS, 402, L72
- Wallerstein, G. & Sneden, C. 1982, ApJ, 255, 577

Appendix A: Parameters and abundances

Table A.1. Measured atmospheric parameters and abundances for stars in the 5 globular clusters. Stetson IDs, V, and I magnitudes are from Stetson et al. (2019).

Gaia Source ID	Stetson ID	T _{eff} (K)	log g (dex)	v _t (km/s)	Flag A(Li)	A(Li) _{NLTE} (dex)	[Na/Fe] _{NLTE}	Vmag	Imag	SNR
NGC4590 ⟨[Fe/H]⟩ = −2.34 ± 0.10										
3496356167836934016	67010	4780	1.68	1.67	<	0.53	-0.28	14.832	13.775	260.4
3496368228105102720	43508	4809	1.72	1.66		0.41	0.46	14.851	13.807	267.7
3496369254600313728	26784	4493	1.02	1.92	<	0.05	-0.02	13.7	12.501	439.5
3496369877372570752	41758	4866	1.87	1.62		0.79	-0.35	15.158	14.139	233.6
3496371183042641152	59548	4896	1.93	1.59		0.91	0.4	15.28	14.274	209.4
3496372931092316288	40799	4140	0.52	2.19	<	-0.65	-	12.673	11.252	760.1
3496366338319493504	24032	4827	1.6	1.7	<	0.5	-0.3	14.409	13.373	306.4
3496399422451210624	75588	4873	1.86	1.62		0.78	0.49	15.122	14.106	215.6
3496371079963753088	77334	4957	2.15	1.52		0.78	0.34	15.763	14.782	161.2
3496394616384561664	79098	4712	1.51	1.73	<	0.43	0.26	14.511	13.423	290.8
3496375684168708096	40678	4139	0.52	2.19	<	-0.67	-	12.717	11.295	783.7
3496375203132394112	69220	4942	2.1	1.54		0.87	0.15	15.66	14.673	184.2
3496371973316933888	70630	4892	1.95	1.59		0.96	0.1	15.344	14.336	197.9
3496372106461287936	73969	4845	1.71	1.66	<	0.57	-0.61	14.716	13.688	275.6
3496371664079202944	73337	4952	2.1	1.54		0.99	0.33	15.621	14.638	171.3
3496373244626964096	31721	4871	1.7	1.66	<	0.56	0.41	14.615	13.598	297.1
3496374687736171392	36851	4857	1.86	1.62		0.84	0.48	15.151	14.128	222.0
3496373210267235968	34954	4400	0.88	2.0		-0.52	-	13.348	12.097	567.1
3496374786518184960	36489	4954	2.07	1.55		1.0	0.03	15.527	14.545	185.2
3496372935389301888	37517	4769	1.61	1.69		0.3	-0.21	14.672	13.61	285.7
3496374000541223040	28713	4687	1.45	1.75	<	0.35	0.33	14.405	13.305	326.2
3496373760023015936	22693	4745	1.59	1.71		0.41	-0.45	14.646	13.573	202.2
3496374619014696704	49051	4957	2.05	1.56		0.93	0.3	15.47	14.489	205.0
3496374649080244096	50919	5252	2.98	1.21	<	1.4	0.43	17.54	16.671	82.0
3496374649080247808	52127	5289	3.06	1.19	<	1.45	-0.59	17.736	16.88	79.6
3496374653376525952	53030	5026	2.27	1.49		0.98	0.11	15.921	14.968	170.0
3496374653376535424	55788	4989	2.18	1.52		0.86	0.16	15.755	14.787	179.0
3496374962612519808	58277	5171	2.78	1.27	<	1.23	-0.22	17.139	16.241	103.2
3496374962612865152	59742	5252	3.01	1.18	<	1.35	0.15	17.688	16.819	91.9
3496374722095925888	39365	5144	2.6	1.39	<	1.15	0.2	16.62	15.712	119.9
3496374511641271552	40876	5240	2.93	1.23	<	1.35	-0.11	17.43	16.557	89.5
3496374619014475520	46780	5057	2.19	1.52		1.0	0.37	15.654	14.713	177.1
3496374619014599296	49038	5067	2.4	1.46		0.94	0.2	16.2	15.263	149.2
3496374580360787840	58425	5260	2.92	1.25	<	1.35	-	17.313	16.447	94.7
3496374515937475584	42407	4868	1.88	1.61		0.94	0.3	15.19	14.172	218.0
3496374408562059136	43074	4996	2.16	1.52		0.93	0.38	15.705	14.74	176.3
3496374515935103104	45404	4908	1.95	1.59		0.83	-0.03	15.315	14.314	178.3
3496374447215621632	48174	4991	2.06	1.56		1.05	0.16	15.404	14.437	191.4
3496374546001036288	53410	5036	2.26	1.5		0.98	0.5	15.838	14.889	163.3
3496374546001036672	53535	5065	2.31	1.48		0.96	0.61	15.932	14.994	153.4
3496371595357372416	56263	4786	1.63	1.69	<	0.48	0.43	14.673	13.619	295.9
3496371561000005248	64967	5312	3.08	1.19	<	1.48	-	17.736	16.888	78.0
3496371492280322560	56063	4918	2.0	1.58		0.93	-0.23	15.409	14.412	203.4
3496371457920560512	48774	5204	2.79	1.29	<	1.21	-0.16	17.064	16.178	104.1
3496371487984315008	51213	5210	2.85	1.25	<	1.28	0.63	17.261	16.377	97.4
NGC6809 ⟨[Fe/H]⟩ = −1.79 ± 0.10										
6751344034158411264	326335	5174	2.74	1.34		1.01	0.12	15.81	14.82	122.0
6751342453610402048	324080	5235	2.94	1.27	<	1.08	-0.5	16.246	15.278	107.5
6751343995499656320	324051	5179	2.74	1.34	<	0.97	-	15.811	14.823	129.8
6751342556689633792	320469	5324	3.17	1.22	<	1.26	0.49	16.775	15.838	80.0
6751343484402601088	319643	5272	3.03	1.23	<	1.22	0.14	16.509	15.554	79.0
6751391686812938496	315902	5450	3.3	1.2	<	1.36	0.32	17.051	16.156	77.2
6751341109281472768	313156	5359	3.19	1.22		1.13	-0.12	16.801	15.876	81.5
6751390797762448640	311803	5309	2.98	1.29		1.24	-0.13	16.279	15.337	105.2
6751343724920865152	309106	5238	2.87	1.29	<	1.1	0.23	16.144	15.177	106.2
6751341830836349440	308529	5083	2.42	1.44		0.99	0.09	15.182	14.158	155.1
6751392305288190592	307788	5332	3.12	1.23	<	1.2	0.26	16.64	15.706	94.8

Table A.1. Continued.

Gaia Source ID	Stetson ID	T _{eff} (K)	log g (dex)	v _t (km/s)	Flag A(Li)	A(Li) _{NLTE} (dex)	[Na/Fe] _{NLTE}	Vmag	Imag	SNR
6751390763402728064	307656	5347	3.18	1.22		1.2	0.39	16.795	15.866	75.9
6751342140074767232	306943	5456	3.23	1.23		1.46	0.38	16.878	15.985	72.0
6751390656025341056	306141	5297	2.98	1.28	<	1.16	-0.38	16.286	15.34	96.1
6751390660317035008	306056	5318	3.17	1.21	<	1.23	-0.05	16.795	15.856	83.7
6751342140074761600	305242	5067	2.28	1.47		1.13	-0.46	14.851	13.821	206.9
6751340941781941376	305193	5438	3.05	1.28	<	1.28	0.06	16.402	15.503	92.2
6751391038280721664	303831	5029	2.18	1.51		1.12	0.03	14.624	13.579	219.8
6751342110013112960	302916	5215	2.8	1.32		1.2	0.36	15.965	14.99	103.0
6751341903854668800	302540	4981	2.1	1.53		1.09	0.12	14.509	13.445	228.4
6751390694683279744	301860	5026	2.04	1.55		1.13	0.07	14.382	13.336	259.2
6751342208794224512	301300	4804	1.61	1.68		0.24	-0.16	13.529	12.39	403.8
6751341693397940864	300879	5286	3.01	1.25	<	1.2	0.03	16.419	15.469	88.6
6751341319739079168	298844	5318	3.15	1.22	<	1.23	-0.68	16.706	15.767	83.5
6751389144196825856	298790	5266	2.99	1.26	<	1.16	-0.07	16.392	15.435	94.0
6751342174434476032	298598	5289	2.99	1.27	<	1.17	-0.34	16.347	15.398	96.5
6751389144196814464	296015	5330	3.2	1.19	<	1.26	0.52	16.907	15.972	81.7
6751341285379341056	293901	5243	3.0	1.24		1.19	0.08	16.434	15.469	97.4
6751389114135277952	293635	5229	2.59	1.41		1.21	0.24	15.411	14.441	140.7
6751341968275842432	293220	5179	2.63	1.38	<	0.97	0.41	15.608	14.62	134.2
6751390900841793920	292670	5088	2.37	1.46		1.05	-0.21	14.986	13.964	207.9
6751341349799595904	292563	5356	3.21	1.2	<	1.27	0.19	16.922	15.996	81.6
6751391003921076608	292256	4999	2.2	1.51		1.03	-0.63	14.687	13.63	239.3
6751341182300980992	290518	5109	2.53	1.4		0.99	0.15	15.368	14.354	141.9
6751389419074690176	289029	5389	3.2	1.22	<	1.28	-	16.825	15.91	88.9
6751342036995315584	288835	5168	2.64	1.37		1.07	-	15.652	14.66	108.2
6751389182848799360	288516	5321	2.72	1.38	<	1.04	-0.5	15.638	14.7	143.9
6751388972398082816	287053	5306	3.15	1.21	<	1.26	0.42	16.74	15.797	75.4
6751341659038190208	286192	5295	3.0	1.26	<	1.21	-	16.381	15.434	85.9
6751389389007466752	286170	5257	2.83	1.31	<	1.04	0.06	16.033	15.073	128.9
6751389384714938112	286012	5463	2.92	1.35		1.22	-0.17	15.989	15.098	129.2
6751389079769304320	285750	5277	2.91	1.29		1.18	0.31	16.171	15.218	93.9
6751389389007492864	283117	5052	2.16	1.52		1.08	0.06	14.557	13.521	242.0
6751389041117539328	282936	5303	2.82	1.33		1.02	-0.43	15.938	14.994	119.2
6751389389013324416	282347	5274	2.83	1.32		1.21	-0.09	16.006	15.052	118.8
6751391721177129344	282318	5179	2.68	1.35		0.97	0.01	15.718	14.73	145.9
6751389487794135040	282263	5198	2.78	1.33		1.03	-0.57	15.911	14.93	119.7
6751341560257307904	282240	5120	2.46	1.42		1.04	-0.26	15.254	14.244	138.9
6751389075477272448	281826	5383	2.65	1.4		1.14	-	15.439	14.522	129.6
6751390248006850048	281308	5383	3.19	1.23		1.3	0.11	16.777	15.86	84.1
6751389045415866752	280881	5235	2.55	1.42		1.11	0.22	15.282	14.314	142.0
6751389281635697024	280653	5212	2.73	1.35		0.98	0.31	15.758	14.782	136.0
6751389453434385024	279936	5212	2.76	1.35		1.02	0.01	15.803	14.827	136.3
6751389453434382464	279541	5315	2.81	1.34		1.16	-0.39	15.891	14.951	103.9
6751389281635686528	278571	5218	2.76	1.35		1.12	-0.39	15.81	14.836	127.7
6751389251574759552	277507	5289	3.04	1.23		1.18	0.14	16.521	15.572	95.2
6751389453434371456	277070	5152	2.51	1.41		1.05	0.11	15.301	14.303	167.8
6751389251568413056	276681	5410	2.9	1.33		1.27	-0.24	16.022	15.114	110.5
6751388564373105920	275964	5263	2.81	1.33		1.14	0.26	15.946	14.988	106.8
6751389354653600384	275405	5315	2.97	1.29	<	1.16	0.05	16.251	15.311	101.6
6751388667455550848	274415	5324	3.21	1.18	<	1.31	-	16.957	16.02	73.0
6751388564380202368	273315	5131	2.56	1.4	<	0.93	0.37	15.421	14.415	135.7
6751389247275926272	273262	5422	3.18	1.25	<	1.33	0.46	16.722	15.818	79.9
6751388560081158656	273227	5144	2.58	1.4		1.08	0.06	15.454	14.453	107.8
6751388628800630272	271839	5327	3.19	1.2	<	1.3	-	16.875	15.939	72.7
6751388663160365312	270899	5330	3.02	1.26	<	1.21	-0.33	16.419	15.484	93.8
6751389320294242944	270742	5185	2.59	1.4	<	0.92	0.29	15.446	14.46	152.8
6751388873617246464	269381	5356	3.08	1.25		1.08	-	16.546	15.62	84.8
6751390518588716160	268772	5263	3.0	1.25	<	1.13	-0.38	16.43	15.472	99.2
6751395225866017536	267230	5353	3.19	1.21	<	1.26	0.06	16.819	15.892	86.5
6751388457001828864	266435	5318	3.15	1.22	<	1.27	0.39	16.713	15.774	77.2

Table A.1. Continued.

Gaia Source ID	Stetson ID	T _{eff} (K)	log g (dex)	v _t (km/s)	Flag A(Li)	A(Li) _{NLTE} (dex)	[Na/Fe] _{NLTE}	Vmag	Imag	SNR
6751388938038247040	264847	5120	2.37	1.46		0.95	-0.12	14.971	13.961	173.3
6751390591604327168	264022	5096	2.43	1.43		1.06	-0.05	15.204	14.185	151.4
6751294586192199424	260457	5246	2.85	1.29	<	1.12	-0.24	16.108	15.144	98.7
6751388731879732864	260403	5226	2.86	1.28		1.16	-0.15	16.146	15.175	98.2
6751389698245827456	260043	5286	3.14	1.21		1.28	0.1	16.741	15.791	131.9
6751388907977025280	260039	5196	2.76	1.34	<	1.04	-0.33	15.822	14.84	112.4
6751389663892790912	259514	5235	2.66	1.37		1.31	-0.34	15.634	14.666	113.6
6751390140629070208	259067	4873	1.8	1.63		0.48	0.15	13.891	12.782	335.6
6751389968830367872	255421	5232	3.03	1.21		1.19	0.01	16.575	15.606	94.3
6751389728312198144	255015	5274	2.97	1.27		1.12	-0.34	16.306	15.352	104.1
6751390415505772672	249222	5212	2.86	1.28		1.02	0.2	16.151	15.175	114.6
6751389934470118272	247467	5210	2.93	1.26	<	1.12	-0.04	16.266	15.289	93.6
6751393370443742080	247265	5204	2.96	1.25	<	1.09	0.11	16.364	15.385	98.6
6751389831390224256	245323	5218	2.99	1.23	<	1.11	0.09	16.447	15.473	95.8
6751294895432000512	245081	5141	2.64	1.37		0.88	0.32	15.685	14.683	132.1
6751392958126845568	245026	5254	3.07	1.21	<	1.23	0.11	16.659	15.698	74.7
6751392958126849024	240566	5254	3.05	1.21		1.23	-0.13	16.62	15.659	93.0
6751389865750374784	239906	5182	2.95	1.24		0.84	0.05	16.378	15.391	111.3
6751295999240906752	236052	5049	2.44	1.43		0.93	-0.17	15.286	14.249	180.2
NGC6656 ([Fe/H]) = -1.77 ± 0.12										
4077588663251815680	368904	4860	1.81	1.62		0.94	-0.27	14.443	13.044	252.5
4077588658876838272	377616	4981	1.98	1.58		0.84	-	14.629	13.287	224.9
4077588761956054656	379517	5207	2.25	1.5		1.09	-0.13	15.147	13.89	172.4
4077588560086108800	410829	4823	1.74	1.64		1.0	-0.35	14.193	12.822	283.2
4077588590157385856	412896	5005	2.07	1.55		0.95	0.04	14.811	13.515	182.3
4077588590157388160	416194	5335	2.37	1.47	<	1.14	0.65	15.251	14.071	141.4
4077588628892104960	350337	4881	1.8	1.63		0.88	0.18	14.231	12.871	255.5
4077588457007213184	373829	5230	2.04	1.55		1.09	0.45	14.577	13.341	213.8
4077588383998945792	398364	5200	2.04	1.55		1.08	0.83	14.646	13.394	218.4
4077588491374970880	408580	4933	1.87	1.6		0.86	0.37	14.376	13.043	242.4
4077588487078079488	414857	4964	1.83	1.61		0.89	0.66	14.091	12.785	250.9
4077588521437920896	430379	5315	2.11	1.55		1.15	-	14.493	13.318	228.9
4077588418358572160	357743	5174	2.1	1.54		1.02	-	14.812	13.556	211.9
4077588418358573824	364260	5021	2.13	1.53		0.89	0.33	15.061	13.744	180.3
4077588422647379584	370752	5057	2.28	1.48		0.91	-	15.301	13.993	171.0
4077588353927668608	378794	4990	2.17	1.51		0.74	-	15.241	13.895	181.2
4077588383998846592	389508	4848	1.79	1.63		0.78	0.18	14.409	13.001	257.5
4077588383998852736	397395	4887	1.82	1.62		0.98	-0.41	14.384	13.003	227.7
4077588388287066112	399172	5150	2.01	1.57		0.91	0.76	14.488	13.219	234.4
4077588383998856448	403369	5114	2.08	1.54		0.82	0.54	14.804	13.527	191.2
4077587632372496384	416210	4942	2.21	1.5		0.9	0.2	15.347	14.001	161.2
4077587731163850624	432474	5096	2.1	1.54		1.01	0.42	14.817	13.555	197.2
4077494513194645248	370100	4947	1.81	1.62		1.01	0.01	14.123	12.775	294.7
4077494513194647936	376994	5391	2.67	1.4		1.1	0.58	15.748	14.553	139.2
4077588349639105664	384662	4992	1.85	1.6		0.94	0.57	14.266	12.913	271.6
4077588354014015616	390011	4939	2.0	1.57		0.8	-0.37	14.825	13.457	218.0
4077587628084617984	411350	5079	2.0	1.57		1.1	-0.27	14.582	13.281	209.2
4077587529292978560	414393	5332	2.87	1.33	<	1.2	0.55	16.246	15.043	113.7
4077587563652581248	432135	5055	2.46	1.43	<	0.93	0.2	15.731	14.43	132.8
4077587662444374016	432601	5179	2.23	1.5		1.04	0.47	15.11	13.857	169.0
4077494483219998336	360399	5286	2.46	1.45		1.15	-0.03	15.421	14.206	160.9
4077587593724864512	389612	5210	2.1	1.54		1.22	-0.23	14.815	13.564	203.2
4077497644316147840	276208	5168	2.73	1.32	<	1.08	-0.43	16.242	14.994	113.7
4077591996146712320	283673	5076	2.59	1.38		1.0	0.51	16.139	14.833	114.4
4077497747395400448	276100	5131	2.54	1.41	<	0.99	-0.68	15.757	14.49	136.2
4077497708642558464	260869	5106	2.09	1.54		1.04	0.51	14.819	13.54	215.3
4077592511542754816	358787	5241	2.88	1.29		1.08	0.52	16.507	15.284	96.6
4077591789902826112	356349	5171	2.81	1.28	<	1.15	0.44	16.471	15.236	95.0
4076836352399393408	481388	5202	2.81	1.3	<	1.2	-	16.368	15.144	94.9
4077591819965737600	372658	5122	2.75	1.29		1.08	0.4	16.371	15.132	88.0

Table A.1. Continued.

Gaia Source ID	Stetson ID	T _{eff} (K)	log g (dex)	v _t (km/s)	Flag A(Li)	A(Li) _{NLTE} (dex)	[Na/Fe] _{NLTE}	Vmag	Imag	SNR
4077493967753050752	314736	5054	2.66	1.28		0.93	0.08	16.333	15.09	107.1
4077497777360246016	300161	5202	2.79	1.31	<	1.16	0.6	16.273	15.053	102.8
4077592202305011584	375932	5164	2.74	1.32		1.11	0.33	16.233	15.003	109.9
4077494654948461824	313278	5188	2.71	1.35		1.05	0.19	16.106	14.868	110.2
4077587662444381952	444075	5187	2.7	1.35		1.1	0.24	16.098	14.853	98.8
4077588113495723008	481069	5191	2.7	1.36		1.28	0.43	16.052	14.819	107.4
4077590617373368064	475444	5099	2.59	1.38		0.75	0.45	16.073	14.776	113.8
4077589006771268864	447304	5132	2.63	1.37		0.81	-0.54	16.019	14.767	121.3
4077494478834898176	352147	5141	2.61	1.38		1.13	0.39	15.948	14.689	121.3
4077588968106307712	432629	5177	2.68	1.36	<	1.1	0.6	15.988	14.768	110.7
4077591648174052224	324068	5109	2.57	1.39		0.8	0.63	15.931	14.66	120.8
4077493727234677760	368201	5134	2.57	1.4		1.11	0.33	15.855	14.592	121.6
4077589316000968192	445345	5272	2.73	1.36		1.17	0.01	15.947	14.739	105.7
4077592202219665280	380144	5090	2.59	1.38	<	1.0	0.4	15.966	14.711	115.8
4077494380069993856	339684	5083	2.56	1.39		0.8	0.12	15.928	14.665	126.9
4077591648165458304	325389	5144	2.6	1.39	<	1.01	-0.17	15.898	14.64	129.2
4077588761956051968	375635	5130	2.55	1.4		0.99	0.21	15.847	14.568	130.6
4077493280556921600	409713	5049	2.52	1.4		0.9	0.43	15.847	14.601	126.9
4077592129201872512	314072	5083	2.53	1.4		0.82	0.64	15.855	14.579	126.5
4077588079048728192	470314	5084	2.53	1.4		0.82	0.47	15.83	14.565	117.7
4077588938043174912	447899	5049	2.49	1.41		0.97	0.33	15.81	14.53	131.3
4077494822424525952	303010	5087	2.52	1.41	<	1.09	0.45	15.764	14.504	97.5
4077493727305709184	362412	5290	2.66	1.39		1.28	0.25	15.689	14.491	129.7
4077592271024514176	370654	5044	2.48	1.41		0.88	0.11	15.802	14.515	135.1
4077494861110024448	322055	5147	2.55	1.4		1.03	0.25	15.724	14.475	137.5
4077589105544866432	447306	5156	2.56	1.4		0.99	0.29	15.739	14.497	116.3
4077587421917657984	472852	5076	2.47	1.43		0.97	-0.23	15.683	14.394	106.2
4077591824347848064	370494	5223	2.61	1.4		1.01	0.2	15.669	14.458	133.0
4077587563652352384	427901	5222	2.54	1.42		0.95	0.48	15.619	14.375	133.6
4077591648174053376	332770	5031	2.41	1.44		0.78	0.03	15.632	14.336	137.3
4077591824262504192	369580	5211	2.56	1.41		1.03	-0.55	15.581	14.372	127.9
4077591923043403648	305397	5317	2.5	1.43		1.17	0.46	15.511	14.299	120.3
4077587357581444480	442522	5047	2.38	1.45	<	0.93	0.12	15.538	14.226	140.0
4077494822432267904	323639	5319	2.52	1.43		1.05	0.67	15.489	14.301	147.3
4077493413674983552	420886	5096	2.47	1.43		0.73	-	15.534	14.289	150.1
4077493555506972416	365795	5082	2.45	1.43		1.03	-0.43	15.511	14.266	144.6
4076742584671349248	429983	5158	2.49	1.43		1.06	-0.04	15.464	14.245	156.3
4077587662436171136	447193	5045	2.36	1.46		0.86	0.04	15.473	14.172	137.1
4077588143480814720	456131	5093	2.43	1.44		0.88	0.52	15.462	14.208	139.6
4077588834965047424	360069	5125	2.44	1.44		0.92	0.61	15.462	14.202	145.4
4077587391853159552	469946	5071	2.38	1.46		0.93	0.59	15.454	14.163	136.2
4077588143472508544	452973	5071	2.39	1.45	<	0.98	-	15.432	14.166	125.1
4077591682533796864	345027	4985	2.27	1.48		0.93	0.11	15.327	14.01	158.9
4077587524997281152	411988	4987	2.16	1.51	<	0.8	-	15.16	13.84	171.5
4077494753712791424	324783	5088	2.22	1.5		0.7	0.7	15.122	13.852	187.7
4077494856782482304	322939	5344	2.23	1.5		1.19	0.58	15.05	13.868	169.6
4077588525812688896	439821	5196	2.11	1.53		0.91	0.83	14.764	13.547	184.2
4077493967823900544	324422	5046	2.07	1.55		1.01	0.22	14.722	13.467	205.9
4077494444467310592	330527	4931	1.98	1.58		0.64	-	14.679	13.344	240.4
4077591888683618816	350137	4901	1.93	1.58		0.85	-0.41	14.618	13.273	213.7
4077591751253266816	317142	4930	1.91	1.59		1.0	-0.61	14.525	13.174	233.2
4077589144288088448	461833	4905	1.88	1.6		0.65	0.69	14.479	13.129	212.4
4077494375780165120	332065	4925	1.89	1.59		0.89	0.52	14.385	13.071	255.3
4077587288861927808	445577	4918	1.84	1.61		0.94	-0.03	14.345	12.989	222.0
4077588800612974848	410770	4894	1.85	1.61		0.87	0.52	14.355	13.025	250.5
4076837112684613504	513824	5124	2.69	1.33	<	1.06	0.44	16.291	15.011	106.5
4077588212192057856	498572	5046	2.3	1.48		0.71	0.55	15.291	14.001	156.2
4076836803447012864	500055	5002	1.99	1.58		0.77	0.44	14.587	13.273	224.7
NGC3201 ([Fe/H]) = -1.58 ± 0.06										
5413528757309438976	117898	4966	2.18	1.5		0.86	-	15.338	14.081	138.2

Table A.1. Continued.

Gaia Source ID	Stetson ID	T _{eff} (K)	log g (dex)	v _t (km/s)	Flag A(Li)	A(Li) _{NLTE} (dex)	[Na/Fe] _{NLTE}	Vmag	Imag	SNR
5413574764994407296	60587	5037	2.49	1.39	<	1.07	-0.19	15.892	14.727	112.4
5413576620427026688	62920	5215	2.8	1.31		1.24	0.29	16.651	15.462	78.6
5413574936799800960	64905	4910	2.05	1.53		0.76	-	15.184	13.9	119.9
5413576757865689472	65575	5028	2.44	1.41		1.04	-0.09	15.946	14.71	105.8
5413576757860772352	67621	5046	2.35	1.45		1.19	-0.17	15.647	14.417	105.8
5413573528050401920	67864	5099	2.62	1.37	<	1.17	0.41	16.139	15.0	100.3
5413577165872587904	68916	4982	2.26	1.47		0.86	-	15.546	14.294	125.8
5413573562410144896	69996	4782	1.75	1.64		0.54	-0.33	14.371	13.096	232.6
5413573940367652736	70894	5193	2.99	1.24	<	1.36	-	16.94	15.838	69.3
5413576547403214336	74008	5071	2.57	1.38		1.12	0.17	16.117	14.913	96.3
5413573974727042944	74399	5047	2.39	1.44	<	1.03	0.48	15.616	14.457	125.4
5413576586067387904	74864	5007	2.24	1.47		1.1	-0.09	15.452	14.234	128.6
5413573145784283520	74998	5123	2.72	1.33		1.26	0.24	16.364	15.228	87.1
5413573493690665728	75717	5092	2.86	1.24	<	1.28	-0.12	16.824	15.676	72.0
5413573867339062144	76722	5174	2.87	1.27	<	1.34	0.42	16.711	15.596	77.3
5413574073501937408	77070	5041	2.38	1.44		1.03	0.19	15.646	14.461	125.4
5413574039142213120	81284	5163	2.84	1.28	<	1.33	0.3	16.75	15.59	76.4
5413576998384278784	81845	4993	2.16	1.51		0.82	-	15.176	13.979	150.2
5413573661180542848	81952	5173	2.9	1.26	<	1.36	-0.04	16.76	15.645	74.1
5413573665489370624	82941	5193	2.83	1.29		1.29	-0.01	16.604	15.496	77.7
5413576891000614272	83375	4921	2.09	1.52		1.04	-	15.125	13.899	145.8
5413576517347896192	83561	5054	2.47	1.4		1.16	-0.31	15.911	14.717	86.5
5413576895305030144	84320	5069	2.48	1.4	<	1.14	0.31	15.87	14.698	102.3
5413576891000617088	85224	5028	2.52	1.39		0.94	-0.26	15.979	14.799	83.3
5413576929664797056	85420	5114	2.69	1.33		1.23	-0.14	16.332	15.184	83.8
5413576139390780160	88006	5022	2.41	1.43	<	1.06	0.33	15.817	14.604	113.7
5413576139385749248	88986	5182	2.76	1.33		1.23	0.23	16.39	15.258	83.1
5413577067103768448	90932	4989	2.19	1.5		1.08	-	15.23	14.032	149.3
5413573837288105984	91115	5099	2.51	1.4		1.03	-0.2	15.912	14.74	114.4
5413573734208868096	91828	5058	2.43	1.42	<	1.09	0.39	15.783	14.604	113.9
5413575314756912768	93635	4970	2.21	1.49		0.77	-0.0	15.426	14.173	139.1
5413573768568647552	94417	5076	2.43	1.42		1.04	0.35	15.826	14.627	92.5
5413526657058305152	94562	5185	2.82	1.29	<	1.36	-0.11	16.683	15.524	75.0
5413576070671310720	96397	5001	2.3	1.46		0.94	-0.44	15.552	14.329	121.8
5413575447891536256	96886	4895	2.12	1.51		0.95	-0.09	15.311	14.017	151.8
5413575447891536896	97114	5027	2.42	1.42	<	1.09	-0.08	15.905	14.658	106.3
5413582186704791168	97812	4937	2.03	1.54		1.63	-	15.029	13.81	163.3
5413575241728645120	97963	4833	1.89	1.58		0.98	0.34	14.846	13.54	189.6
5413575447891539072	98029	5028	2.29	1.46		1.07	-0.15	15.565	14.328	126.9
5413575280397190016	99159	4985	2.33	1.45		0.89	-	15.644	14.402	127.3
5413575894568230656	101600	5071	2.84	1.25	<	1.14	-0.14	16.949	15.72	62.4
5413575383476473088	101793	4999	2.31	1.45		0.84	-	15.638	14.387	114.7
5413575276092858368	101809	5048	2.47	1.4		1.0	-0.1	15.979	14.759	105.5
5413575379172073856	102080	5126	2.44	1.41	<	1.15	-0.13	15.834	14.639	111.6
5413576001951864064	104083	4989	2.29	1.46		1.09	-0.02	15.636	14.369	124.9
5413581907522447488	104928	4987	2.15	1.51		1.03	-0.4	15.244	14.01	142.9
5413575933232381696	106829	5077	2.56	1.39	<	1.18	0.09	16.151	14.924	93.1
5413528482431516672	107985	5041	2.46	1.4		0.99	-0.19	15.972	14.745	108.3
5413528787362489856	110428	5053	2.46	1.4		1.09	-0.2	15.987	14.755	100.2
5413528791669165440	110970	5004	2.38	1.44		0.91	0.35	15.771	14.523	131.9
5413529032187348608	111064	5122	2.79	1.3	<	1.28	0.09	16.677	15.47	79.9
5413528826028906880	113875	4949	2.05	1.53		0.95	-	15.158	13.895	159.1
5413577548139593984	43732	5177	2.88	1.27	<	1.44	-0.26	16.692	15.593	63.5
5413577685578562944	45453	5249	2.92	1.28	<	1.43	-	16.69	15.61	73.8
5413577616859080960	47619	5221	2.9	1.27	<	1.44	0.15	16.701	15.61	67.0
5413574421403594240	51296	5233	3.0	1.25	<	1.44	0.04	16.903	15.822	69.8
5413574558842563328	54279	5133	2.77	1.32		1.28	-0.06	16.399	15.291	84.7
5413574971159438592	56935	5198	2.84	1.28	<	1.35	0.23	16.607	15.509	79.1
5413579678443436288	57259	4971	2.31	1.45		1.07	-0.33	15.644	14.388	123.1
5413576482988137600	80609	4993	2.3	1.45		0.93	-	15.567	14.338	126.1

Table A.1. Continued.

Gaia Source ID	Stetson ID	T _{eff} (K)	log g (dex)	v _t (km/s)	Flag A(Li)	A(Li) _{NLTE} (dex)	[Na/Fe] _{NLTE}	Vmag	Imag	SNR
5413576379903287680	74438	5122	2.79	1.3		1.21	-0.32	16.632	15.445	80.5
5413575761428289664	83738	5068	2.25	1.47		1.01	-0.04	15.436	14.233	137.6
5413575722769510528	83906	4955	2.01	1.55		0.91	-	15.009	13.763	160.7
5413575692714165888	90831	4971	2.34	1.45		1.11	-0.22	15.666	14.427	123.2
5413576341244664448	75098	5107	2.31	1.46		0.97	-	15.527	14.328	128.7
5413576375604411136	78059	4957	2.05	1.53		0.98	-0.25	15.155	13.895	151.2
5413575619690179072	81662	5064	2.39	1.44	<	1.07	0.04	15.725	14.518	121.5
5413575722769408896	86611	5076	2.44	1.41	<	1.11	0.47	15.859	14.657	112.7
5413575658348856192	89130	5087	2.6	1.38	<	1.19	-	16.211	15.017	95.7
5413575692714152192	90541	4943	2.0	1.55		0.74	-	15.023	13.76	173.0
5413575589634849408	77604	5028	2.35	1.45	<	1.01	0.41	15.612	14.399	129.5
5413575623988713984	78651	4965	2.05	1.53		0.72	-	15.125	13.879	163.9
5413575585330436608	80314	5020	2.31	1.45	<	0.99	-0.12	15.538	14.332	132.0
5413575550970716928	86502	5030	2.22	1.48		1.17	-0.39	15.385	14.171	137.8
5413575654049935360	87245	5118	2.45	1.41		1.1	0.13	15.871	14.673	111.0
5413575447891531008	95041	5063	2.51	1.39		0.93	-0.21	16.055	14.826	108.1
5413574863775897216	69121	5044	2.43	1.41		0.78	0.29	15.837	14.644	118.3
5413574863775908736	73445	5032	2.36	1.45		1.11	-0.23	15.576	14.383	133.0
5413574863775910784	73955	5076	2.74	1.32	<	1.22	0.12	16.489	15.314	83.3
541357555275124352	90802	4952	2.21	1.49		0.98	-	15.504	14.221	118.9
5413574043446583552	82836	5023	2.4	1.44		0.9	-0.18	15.813	14.574	121.4
5413575349116671744	91356	5061	2.61	1.37		1.2	-0.2	16.321	15.09	92.7
NGC6838 <[Fe/H]> = -0.72 ± 0.07										
1821606719608983552	159767	5007	2.3	1.44		0.87	-	15.181	13.938	198.1
1821607028846759936	139910	5053	2.61	1.32		0.76	-	16.059	14.834	131.8
1821606921430534144	132783	4872	2.21	1.44	<	0.83	-	15.307	14.008	176.3
1821618642439491072	123258	4890	2.23	1.44		0.74	-	15.295	14.004	183.4
1821608849912747904	189653	5082	2.39	1.39		0.82	-	15.65	14.436	148.5
1821608781193211392	195102	5095	2.4	1.39		0.88	-	15.681	14.472	144.9
1821609124790724736	184627	4997	2.29	1.44		0.85	-	15.219	13.972	172.9
1821608918632106368	212643	5103	2.46	1.36	<	1.04	-	15.905	14.699	135.0
1821614862867880192	206187	5159	2.41	1.37		1.19	-	15.823	14.638	138.3
1821620978901638144	177436	4995	2.29	1.44		0.91	-	15.235	13.987	188.3
1821620978901633152	178029	4950	2.28	1.43		0.92	-	15.337	14.071	178.1
1821608334516883968	182638	5236	2.43	1.32		1.07	-	16.053	14.896	128.9
1821607990919181696	196866	4921	2.36	1.4		0.73	-	15.607	14.329	158.3
1821607200645158400	190514	5079	2.91	1.23	<	1.09	-	16.423	15.208	79.2
1821605894975152128	175885	5025	2.41	1.39		0.82	-	15.701	14.465	158.1
1821627232374952704	170015	4881	2.24	1.44		0.98	-	15.353	14.058	186.1
1821620326067079680	151882	5124	2.38	1.42	<	0.98	-	15.425	14.227	167.9
1821620772743302912	139388	4924	2.59	1.34		0.82	-	16.012	14.735	127.0
1821609120458083456	185301	5030	2.38	1.41		0.67	-	15.541	14.307	157.4
1821620841462681984	167131	4948	2.31	1.42		0.88	-	15.43	14.163	162.6
1821609051738460288	187503	5159	2.67	1.27		1.09	-	16.192	15.007	117.7
1821620424811791744	155286	5095	2.86	1.25	<	1.1	-	16.309	15.1	109.6
1821608712473894784	169861	5124	2.5	1.34		0.95	-	15.979	14.781	136.4
1821608643720219776	174250	4973	2.29	1.43		1.0	-	15.273	14.016	180.7
1821608433263154176	180780	4973	2.31	1.43		0.75	-	15.375	14.118	173.3
1821608815518575872	184337	5103	2.54	1.34		0.94	-	15.986	14.78	139.1
1821608811220291200	187296	5197	3.08	1.21	<	1.22	-	16.594	15.423	99.7
1821608605061812224	166246	5079	2.38	1.42		0.74	-	15.448	14.233	176.5
1821608433263141248	174895	5151	2.4	1.39		1.12	-	15.634	14.446	150.7
1821608437595913472	177054	5020	2.37	1.41		0.9	-	15.534	14.296	154.8
1821608437561457536	181230	5124	2.42	1.36		0.97	-	15.874	14.676	136.7
1821608403236176000	173214	5095	2.36	1.44		1.16	-	15.086	13.877	195.7